Applied Thermal Engineering 233 (2023) 121143

Contents lists available at ScienceDirect

Applied Thermal Engineering

journal homepage: www.elsevier.com/locate/apthermeng

Research Paper

Experimental investigation of a novel variable geometry radial ejector

Raed Al-Rbaihat [a,b], Khalid Saleh [a,*], Ray Malpress [a], David Buttsworth [a]

[a] School of Engineering, University of Southern Queensland, Queensland 4350, Australia
[b] Department of Mechanical Engineering, Tafila Technical University, Tafila 66110, Jordan

ARTICLE INFO

Keywords:
Variable geometry
Radial ejector
Experiments
Entrainment ratio
Critical compression ratio
Isentropic ejector efficiency

ABSTRACT

This work focuses on improving ejector performance in variable conditions by developing a radial flow variable geometry radial ejector (VGRE). The research objective was to demonstrate the performance of the improved VGRE, which can operate more effectively under changing operating conditions compared to a fixed geometry design. The improved VGRE was developed and experimentally tested to enable adjustment of the nozzle and ejector throat areas to suit different ejector operating conditions in various applications. Radial ejectors have a smaller size than axial ejectors, which is a significant advantage in some applications. Results showed that the improved VGRE achieved higher entrainment ratio and critical compression ratio compared to a fixed geometry design and that optimal performance was obtained with nozzle and duct throat separations of 0.5 mm and 3.0 mm, respectively. The results also indicated that the wall static pressure in the throat region of the improved VGRE was similar to that observed in conventional axial ejectors and showed an average improvement of 107 % in entrainment ratio and 76 % in critical compression ratio relative to previous studies of air ejectors. The findings suggest that the improved VGRE concept could be applied to a wide range of applications in the future.

1. Introduction

Ejectors have garnered significant interest as a viable technology that can be effectively powered by low-grade energy sources, including solar and waste heat [1–5]. In light of growing concerns regarding the environmental and economic impact of conventional cooling systems, there is an increasing focus on utilizing solar-powered ejector cooling systems for both commercial and residential applications [4,6]. Ejectors can serve as a supplementary component to compressors or even replace the conventional throttling valve in HVAC and refrigeration systems, thereby reducing electric power consumption, especially when coupled with a solar energy source [3,5].

The performance of ejector cooling cycles is typically quantified by the Coefficient of Performance (COP), which typically ranges between 0.2 and 0.8 and heavily relies on the efficiency of the ejector itself [7–9]. While these COP values may be lower compared to conventional vapor compression refrigeration systems, they still prove to be practical and viable, particularly in scenarios where the primary energy source, such as solar insolation, is abundantly available.

To improve ejector performance, various methods have been explored, including control of operating conditions, working fluid properties, and ejector geometry. Conventional axial ejectors are commonly designed with fixed geometry configurations, limiting their performance to a narrow range of operating conditions. However, in solar ejector cooling systems with fluctuating operating conditions driven by variable energy sources and heat sinks, fixed geometry ejectors result in poor performance and cannot fully leverage the fluctuating solar insolation during the day. The sensitivity of cooling systems with fixed geometry ejectors to operating conditions restricts their operational flexibility and commercial viability.

Researchers have investigated the theoretical advantages of incorporating adjustability into ejector cycles. One study demonstrated that a variable geometry ejector could achieve energy savings over 50 % greater than a fixed geometry ejector [5]. Another study highlighted the importance of using a variable-speed pump in the ejector cycle and presented improved performance of a small-scale solar-powered air-conditioning system with a adjustable geometry ejector design, resulting in a 24 % increase in COP and a maximum value of 0.29, along with a cooling capacity of 1.6 kW [10].

There are three main flow areas that have a major impact on ejector performance: primary nozzle throat area, primary nozzle exit area, and ejector throat area. In the case of axial flow ejectors, experimental

* Corresponding author at: School of Engineering, Faculty of Health, Engineering and Sciences University of Southern Queensland, Toowoomba, Queensland, 4350, Australia. Tel.: +61 7 4631 2889.
E-mail address: Khalid.Saleh@usq.edu.au (K. Saleh).

https://doi.org/10.1016/j.applthermaleng.2023.121143
Received 22 March 2023; Received in revised form 25 June 2023; Accepted 8 July 2023
Available online 10 July 2023
1359-4311/

investigations have extensively explored adjustable primary nozzle throats, which typically utilize a spindle to alter the primary nozzle throat area [11–18]. These studies have revealed that the nozzle throat area has a significant impact on ejector performance and system COP [19]. The optimal position of the spindle depends on the specific operating conditions [12,16]. Pereira et al. [20] conducted a study that demonstrated the advantages of variable nozzle throat geometry in a cooling system, achieving an impressive 80 % increase in system COP compared to a fixed geometry ejector. Yapici and Ersoy [21] observed a COP increase of over 50 %, while Al-Nimr et al. [22] reported improvements in both COP and cooling capacity, with maximum enhancements of approximately 56 %, 60 %, and 58 %, respectively. Several other researchers have also reached similar conclusions [23–26].

The primary nozzle exit area and the ejector throat area also have a significant impact on ejector performance, but direct adjustability of these areas cannot be easily arranged in axial flow ejectors. The operating envelope of axial flow ejectors can be broadened by adjusting the primary nozzle position relative to the ejector to the ejector throat [1,16,17,20]. Such adjustments can be viewed as inducing effective changes in the nozzle exit area and the ejector throat area, but direct modulation of these areas has not been demonstrated in axisymmetric axial flow ejectors.

In contrast to axial ejectors, radial ejectors [27,28] offer the advantage of easy adjustment of the nozzle throat and ejector throat area within a single device by altering the separation of the nozzle and duct walls. This makes the Variable Geometry Radial Ejector (VGRE) a promising area of study for enhancing ejector performance [29–32]. Researchers have explored variable geometry ejectors as a solution to improve ejector performance, with studies on rotary radial ejectors by Garris et al. [33] and radial ejectors with rotary nozzles by Tacina et al. [34]. However, issues such as vibration, mechanical failures, and precision requirements have been associated with the rotary concept [35]. Ng and Otis [27] introduced a radial ejector without rotary parts, utilizing a spool, primary diffuser plate, and secondary diffuser plate; they were the first to propose the variable geometry radial ejector (VGRE) concept. Rahimi [28] later revisited the VGRE concept, theoretically allowing for the alteration of nozzle and ejector throat areas through changes in nozzle surfaces and/or duct walls separation. The impact of geometry on radial ejector performance has not been fully examined; further investigation of VGRE geometries could enhance the ejector's overall performance at different operating conditions.

In a conventional axial ejector configuration, the working fluid enters the nozzle and passes through the ejector duct in an axial direction, where the nozzle, suction chamber, ejector throat, and diffuser are all co-axial. However, the scenario in the variable geometry radial ejectors is different: the primary flow expands and accelerates in a supersonic radial flow nozzle, and the expanding disc of the primary flow entrains the secondary flow. The arrangement is illustrated in Fig. 1. The secondary flow enters from both sides of the expanding primary flow. The primary and secondary flows are accelerated principally in the radial direction, and deceleration in the diffuser also occurs in the radial direction; the flow is sandwiched between disc-like surfaces that form the primary nozzle and the ejector duct. The VGRE configuration provides the capability to alter the nozzle and ejector throat areas by changing the separation of the nozzle surfaces and/or duct walls during operation. The radial ejector configuration does not require moving components to achieve the compression and entrainment effects.

Similar to axial ejectors, radial ejector configuration consists of two main parts: supersonic nozzle and ejector duct, as illustrated in Fig. 1. The radial supersonic nozzle has four different sections: uniform cross-sectional area inlet, convergent section, throat, and divergent section. The radial ejector duct consists of a mixing chamber and diffuser. The mixing chamber of the radial ejector configuration consisted of two parallel circular surfaces with a converging region to create a throat.

The focus of this research is the challenge of maximising ejector performance at varying conditions by designing a radial flow ejector with variable geometry. The goal is to improve its efficiency under changing operating conditions, particularly when using renewable energy sources. The main objective is to develop and evaluate the performance of a new and improved radial flow ejector with variable geometry capabilities, referred to as the Improved Variable Geometry Radial Ejector (VGRE). This design builds on the original VGRE concept introduced by Rahimi [28]. Experiments were conducted to assess the performance of the Improved VGRE, and results are compared with a gas dynamics model and previous experimental findings under various conditions.

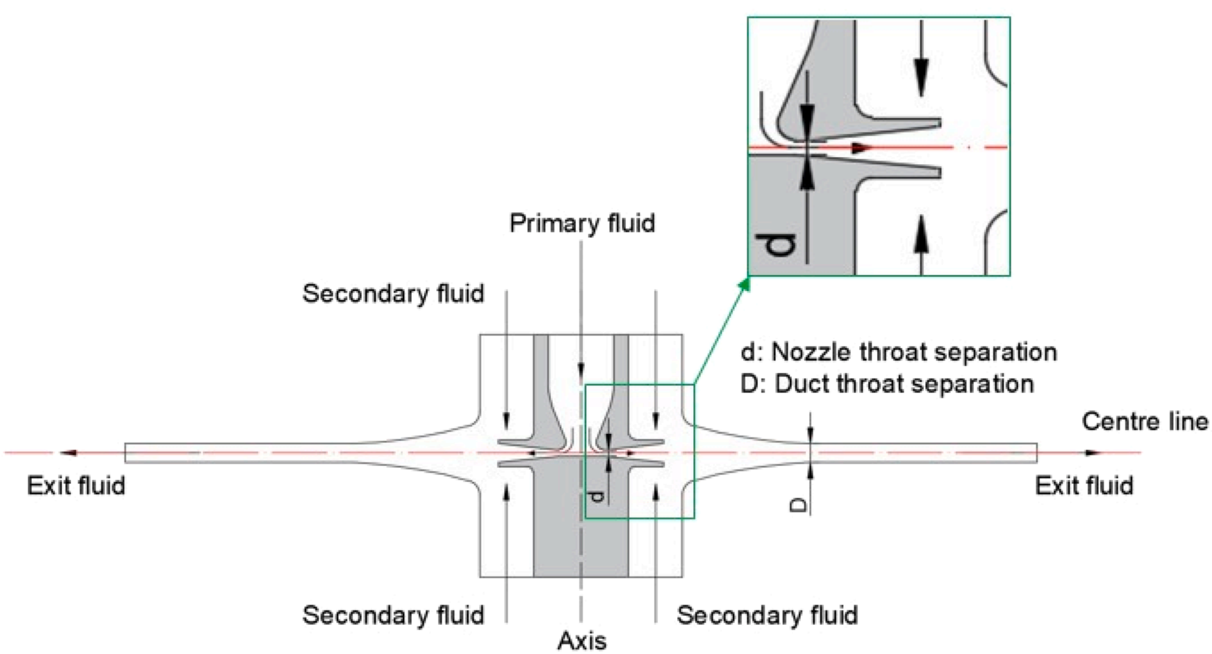

Fig. 1. Schematic diagram of the VGRE configuration showing the nozzle and duct throat separations [36].

2. Ejector performance

Entrainment ratio (ω) and critical outlet pressure (P_o^*) are the most frequently used performance indicators for ejector performance evaluation. The entrainment ratio is defined as:

$$\omega = \frac{\dot{m}_s}{\dot{m}_p} \tag{1}$$

where $\dot{m}_s$ and $\dot{m}_p$ are secondary and primary mass flow rates, respectively.

Critical outlet pressure is the outlet pressure when the entrainment ratio starts to decrease, as the outlet pressure is increased. Higher entrainment ratio and critical outlet pressure generally define higher ejector performance.

The performance of ejectors can also be described by expansion ratio (r_e) and critical compression ratio (r_c^*). The expansion ratio and the critical compression ratio are defined as:

$$r_e = \frac{P_p}{P_s} \tag{2}$$

$$r_c^* = \frac{P_o^*}{P_s} \tag{3}$$

where P_p and P_s are primary and secondary pressures, respectively.

Another important parameter that can be used to describe the performance of ejectors is the ejector isentropic efficiency. The isentropic efficiency of an ejector can be defined as the ideal work required to compress the secondary stream divided by the ideal work obtainable by expanding the primary stream. If the stagnation temperatures of the primary, secondary, and outlet streams are equal, the isentropic efficiency of an ejector (η) based on an ideal gas can be calculated using [37]:

$$\eta = \omega \times \frac{(P_o/P_s)^{\frac{\gamma-1}{\gamma}} - 1}{1 - (P_o/P_p)^{\frac{\gamma-1}{\gamma}}} \tag{4}$$

where $\omega, \gamma, P_p, P_s andP_o$ are the entrainment ratio, specific heat ratio ($\gamma_{air} = 1.4$), primary, secondary and outlet pressures, respectively.

It should be noted that the isentropic efficiency of an ejector takes into consideration the values of the primary, secondary and outlet pressures as well as the primary and secondary mass flow rates. Thus, the overall ejector performance calculated by using the isentropic efficiency of the ejector is a comprehensive ejector performance parameter.

The optimal ejector performance is regarded as the highest achievable entrainment ratio, critical outlet pressure and ejector isentropic efficiency for a given set of operating conditions. The operating conditions, working fluid properties and ejector geometry parameters have a significant influence on ejector performance in terms of entrainment ratio, critical outlet pressure and ejector isentropic efficiency, which are related to the COP and cooling capacity of ejector refrigeration systems.

3. Experimental apparatus

3.1. Improved VGRE

The improved VGRE configuration, shown in Fig. 2, was developed based on the original VGRE [28] based on extensive computational simulations [36,38]. Table 1 presents the equivalent ejector and nozzle area ratios corresponding to the different nozzle and duct throat separations utilized in the experiments of the improved VGRE.

The decision to employ a zero-degree divergent angle in the diffuser section of the radial ejector was based on various factors and recommendations from previous studies [39,40]. Typically, axial ejectors utilize conical subsonic diffusers with divergence half-angles ranging from 3 to 4 degrees, not exceeding 7 degrees. Moreover, it has been suggested to maintain a diffuser area ratio below 5.0 [24,39–44]. Extensive computational fluid dynamics (CFD) investigations confirmed the benefits of maintaining parallel diffuser surfaces after the duct throat and a diffuser area ratio of 1.7. Because of the radial flow, the flow cross sectional area increases even with parallel diffuser surfaces. The choice of parallel surfaces was driven by considerations such as achieving an optimal diffuser length and favourable diffuser arrangement [36], without generating excessive adverse pressure gradients compared to conventional axial ejectors. Future designs may actually require converging surface to reduce disc separation as the radius increases to avoid excessive adverse pressure gradients.

3.2. Apparatus layout

The apparatus was designed to test the performance of the improved VGRE concept. It was equipped with manual adjustors to change the nozzle and/or duct throat separations, allowing for different nozzle and ejector throat areas. The adjustors were easily accessible from outside the ejector and enabled changes to be made within minutes. However, geometry changes could not be made while the rig was operating, meaning tests had to be conducted with a fixed geometry. Although the experiments were conducted at different, fixed, small, stepped increments in geometry, a fully functional variable geometry ejector would allow for continuously variable geometry during operation that could be achieved within seconds to optimize performance under

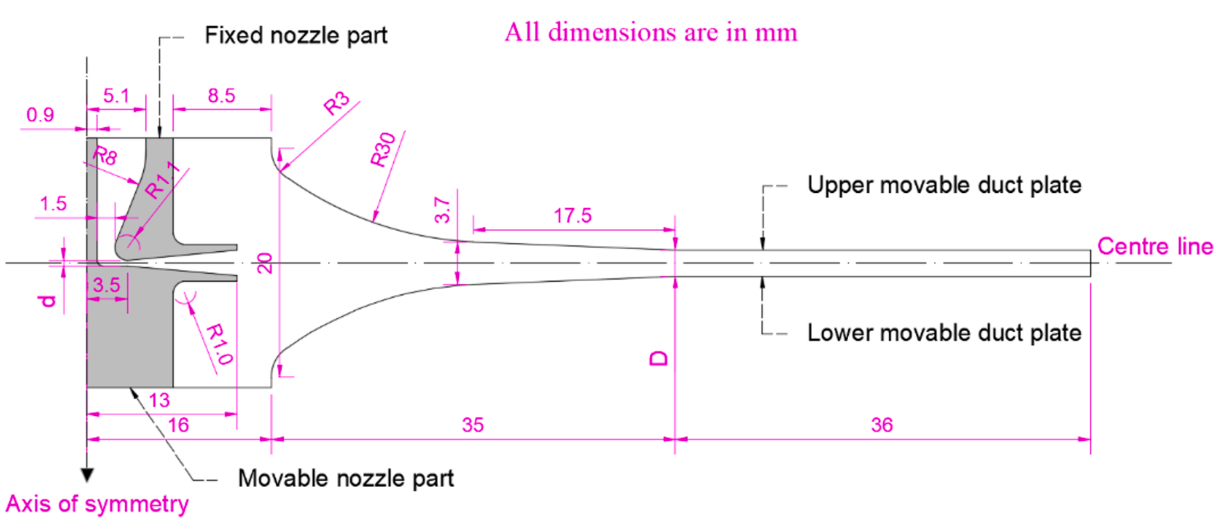

Fig. 2. Schematic diagram of the improved VGRE configuration.

Table 1
Ejector and nozzle area ratios for different nozzle and duct throat separations.

Nozzle throat separation (d) in mm	0.4	0.5	0.6	0.4	0.5	0.6	0.4	0.5	0.6
Duct throat separation (D) in mm	2.3	2.3	2.3	2.6	2.6	2.6	3.0	3.0	3.0
Ejector area ratio (AR)	84	67	56	95	76	63	109	87	73
Nozzle area ratio (AR_n)	19.4	16.4	14.2	19.4	16.4	14.2	19.4	16.4	14.2

various operating conditions. The rig included an improved VGRE, air compressor, vacuum pump, flow control, thermocouples, pressure transducers, data acquisition, receiving tank, vacuum tank, fittings and pipes, and measurement equipment needed to evaluate the system performance. Fig. 3 displays a schematic diagram of the rig setup with control and instrumentation.

The vacuum setup consisted of a large dump tank with a volume of approximately 9 m^3, a main vacuum pump, a secondary vacuum pump, and a vacuum test section equipped with pressure transducers and other measurement instruments. The large dump tank was evacuated to an absolute pressure of around 0.8 kPa by two vacuum pumps, which provided sufficient vacuum volume to run tests for 60–120 s. The test running time was determined by the initial vacuum section pressure, primary pressure, and secondary pressure. The main vacuum pump with high capacity and the secondary vacuum pump with low capacity reduced the turn-around time between experiments to about 30 min.

The design of the ejector system ensured that the dimensions and performance of non-ejector components did not impact the VGRE's performance. The primary and outlet pressure transducers were positioned close to the ejector body, and the secondary pressure transducer was connected directly to the ejector. A photograph of the experimental setup in its operating state, along with its supporting components, is shown in Fig. 4.

3.3. Manufacture of the primary nozzle and ejector duct

The variable radial supersonic nozzle is a crucial component of the improved VGRE system. It is constructed with the upper and lower portions made of Stainless Steel to maintain surface quality and precision, allowing for the necessary small separations to be accurately achieved. Fig. 5 shows a cross-section of the variable radial supersonic nozzle, featuring an extension on the lower portion for axial alignment

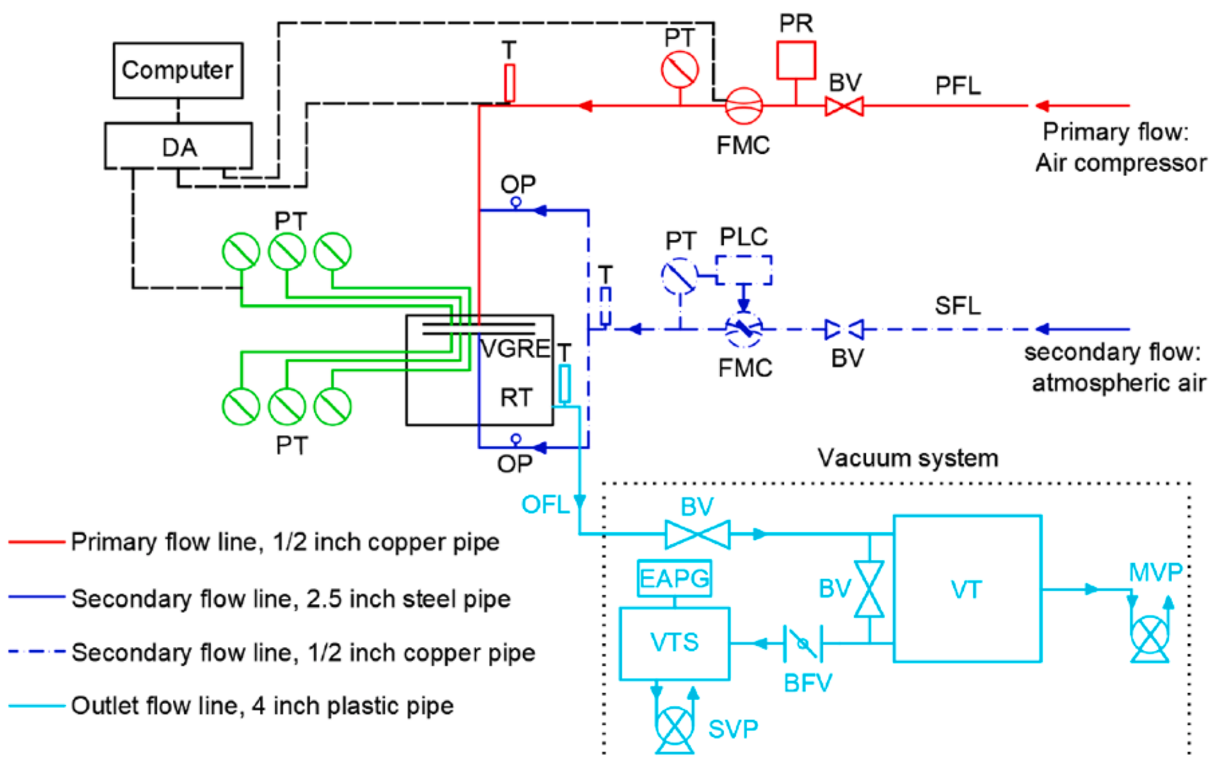

(BFV) Butterfly valve, (BV) Ball valve, (DA) Data acquisition system, (EAPG) Electronic absolute pressure gauge, (FMC) Flow meter controller, (MVP) Main vacuum pump, (OP) Orifice plate, (OFL) Outlet flow line, (PFL) Primary flow line, (PLC) Programmable logic controller, (PR) Pressure regulator, (PT) Pressure transducer, (RT) Receiving tank, (SFL) Secondary flow line, (SVP) Secondary vacuum pump, (T) Thermocouple, (VGRE) Improved variable geometry radial ejector, (VT) Vacuum tank, and (VTS) Vacuum test-section.

Fig. 3. Diagram of the plumbing and instrumentation for the improved VGRE.

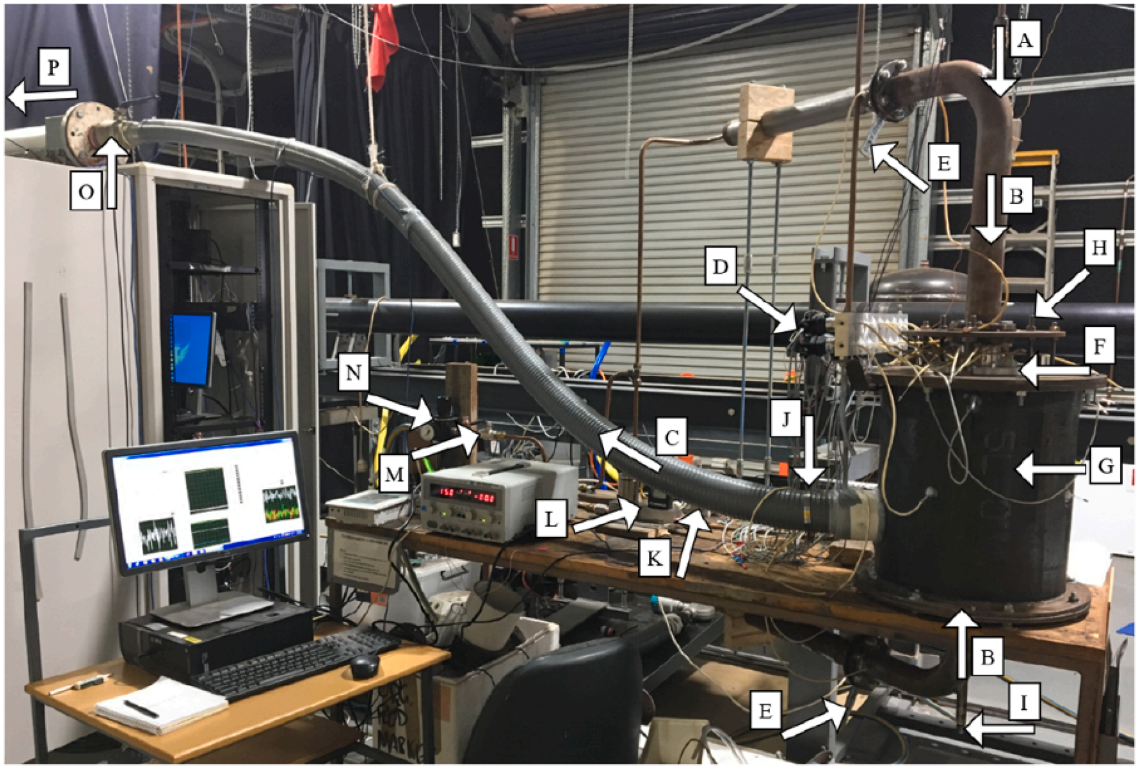

(A) primary supply line, (B) secondary flow line, (C) outlet line connected to vacuum system, (D) pressure transducers, (E) orifice plate, (F) upper ejector duct plate, (G) receiving tank, (H) control rods to adjust the upper ejector duct plate, (I) control rod to adjust the lower nozzle portion, (J) data acquisition system, (K) PLC, (L) flow meter controller, (M) control valve of the primary pressure, (N) pressure regulator, (O) ball valve to access the vacuum system, (P) vacuum system.

Fig. 4. Image depicting the experimental setup along with its auxiliary components.

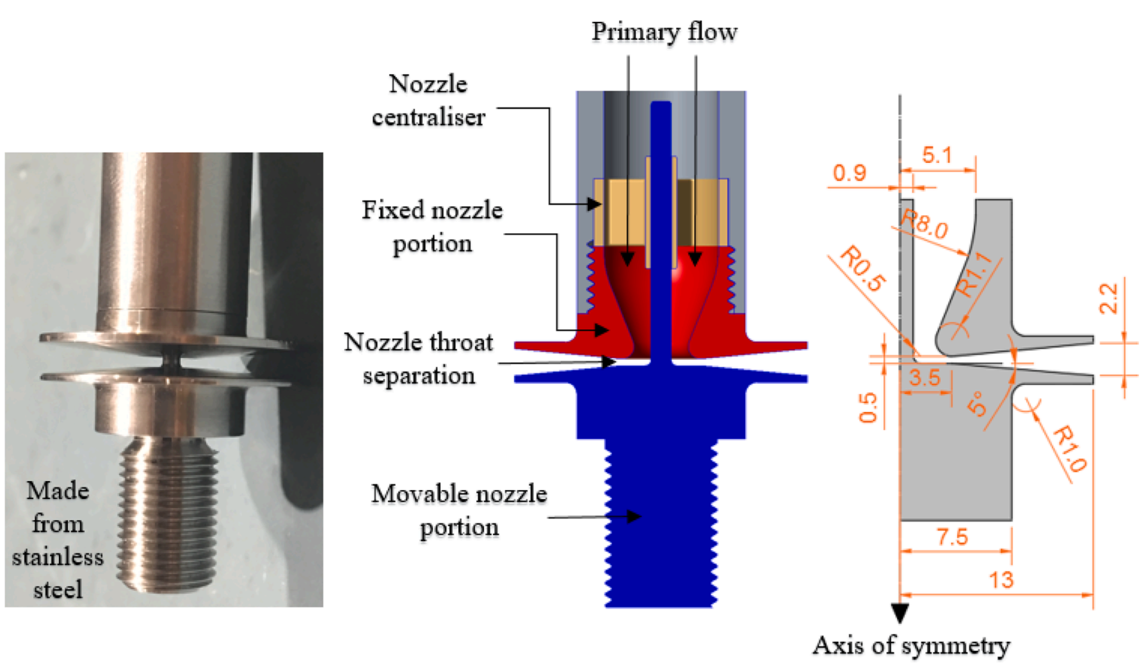

Fig. 5. Diagram indicating the internal components of the supersonic nozzle with variable radial flow. Measurements are expressed in millimetres.

using a centraliser. The experiments were conducted with nozzle throat separations specified at 0.4, 0.5, and 0.6 mm, with a cylindrical throat area of a radius of 3.5 mm. The radial nozzle was designed to have an adjustable area ratio range of 14.2–19.4, and the nozzle throat area of the variable radial ejector was set to be between 8.8 and 13.2 mm^2.

The radial ejector duct is composed of a mixing chamber and diffuser. The design of the mixing chamber in the radial ejector configuration features two mirrored surfaces creating a converging region to form a throat. This design was adopted from the improved VGRE configuration and was based on the CFD results from the original VGRE. The simulations predicted an average improvement of 54 % in the entrainment ratio and 28 % in the ejector isentropic efficiency, with a maximum increase of 16 % in the critical compression ratio. The diffuser was designed with a zero-degree divergent angle, as simulations showed that parallel ducts were optimal. The length of the diffuser was fixed at 36 mm and the flow path length was 87 mm. The duct throat separation of 2.3, 2.6 and 3.0 mm resulted in ejector throat areas ranging from 737 to 961 mm^2 and ejector area ratios of 56–109. The experiments utilized expansion ratios in the range of 89–167. The upper ejector duct plate was connected to the upper secondary line outside the receiving tank, while the lower plate was connected to the lower secondary line within the receiving tank. Both duct plates were made from aluminium to maintain dimensional tolerances and surface finish. Fig. 6 shows a cross-section of the variable radial ejector ducts.

In this experimental work, the specific values of 0.4–0.6 mm and 2.3–3.0 mm were selected for nozzle and duct throat separations, respectively, to balance achieving the desired flow conditions and ensuring an appropriate test duration for accurate measurements. In addition, these dimensions allowed us to observe and evaluate the improved VGRE's performance under realistic operating conditions. Furthermore, while higher values such as 5 mm or 10 mm for nozzle and duct throat separations could be considered, it is important to note that increasing these dimensions would require a corresponding increase in the mass flow rate to achieve supersonic flow conditions necessary for proper ejector operation. This would result in significantly shorter test durations. Additionally, extensive CFD investigations were conducted to determine the best range of nozzle and duct throat separations that improve performance relative to the original VGRE prior to the experiments [36,38]. Based on that, the best range of nozzle and duct throat separations was introduced as a guide to designing the improved VGRE. Meanwhile, experiments revealed that the secondary pressure suddenly raised during the tests resulting in a sharp decline in the secondary mass flow rate for the tests outside the selected range. This resulted in failure performance in a very short time (a few seconds). Table 2 presents comparison details of the geometric parameters of the original VGRE and the improved VGRE.

3.4. The experimental test procedure

Before each test, three key factors were considered: (1) the primary pressure, (2) the secondary pressure, and (3) the initial vacuum pressure. The average time for each test was approximately 5 min, however, the turnaround time could exceed 60 min due to the pumping down of the main vacuum system in case of unexpected operational issues. After each test, both the primary and secondary valves were closed simultaneously to protect the system components.

Table 3 displays the instrumentation used in the ejector system, including the range and measurement technique details. Sixteen Wika model A-10 pressure transducers were used, with one for the primary stream and fifteen for the secondary and outlet streams and duct wall pressures. A FMA-2600A-OMEGA flow meter controller was utilized to measure the mass flow rates, and four type K thermocouples were used: three thermocouples for measurement of the temperature of the primary, secondary, and outlet streams, while the fourth one was used to measure the atmospheric temperature near the apparatus. A pressure regulator was utilized to keep the primary pressure constant during experiments, while a PLC system was used to drive the flow meter controller and to maintain the secondary pressure constant. All signals from the pressure transducers, thermocouples, and flow meter controller were recorded using a National Instruments Compact Data Acquisition system. A flow chart outlining the experimental procedure is shown in Fig. 7, and a list of operating conditions and geometrical parameters is presented in Table 4.

Table 5 presents the experimental results for varying nozzle and duct throat separations. The ejector system design allowed for nozzle area ratios between 14.2 and 19.4, and ejector area ratios between 56 and 109 by adjusting the nozzle and duct throat separations. The data in Table 5 reveals that the primary flow rate remained constant at a given primary pressure for each nozzle throat separation and only changed when the nozzle throat separation was adjusted. The entrainment ratio and the critical outlet pressure varied with different nozzle and ejector area ratios. The maximum deviation in both primary and secondary pressures was less than ± 2.2 %, while the maximum deviation in both primary and secondary temperatures was less than ± 1 %. The temperatures listed in Table 5 for the primary, secondary, and outlet were recorded at the critical outlet pressure. The temperature of the secondary flow was consistently higher than that of the primary flow and remained nearly constant throughout the tests.

3.5. Uncertainty analysis

To validate the results of the experiments, an uncertainty analysis was conducted. The accuracy of the high and low range pressure transducers (Wika 10-A) was determined to be 0.5 % based on the manufacturer's data. The flow meter controller used to measure the primary and secondary mass flow rate had an accuracy of 0.8 %. The temperature of the primary, secondary, and outlet pressures was measured using K-type thermocouples with a precision of 0.7 %. The ambient laboratory temperature was measured using a thermometer with an accuracy of 0.7 %, while the atmospheric pressure was measured using a barometer with a precision of 0.01 %. These accuracy values were obtained from the relevant device user's manuals.

The uncertainty of the measurements was calculated using the root sum of squares method [10]. The uncertainty of the primary, secondary, and outlet pressure was estimated to be ± 0.5 %, while the uncertainty of the mass flow measurements was estimated to be ± 1.2 % for the primary stream and ± 0.8 % for the secondary stream. The uncertainty of the entrainment ratio was estimated to be ± 1.4 %.

The experiments took into account the calibration of the measuring devices, measurement uncertainties, systematic error, system stability, system repeatability, and noise from the electrical and data acquisition systems. It is estimated that the entrainment ratio and critical outlet pressure reported in this work have an accuracy of ± 3 %. The error bars added to the figures represent these uncertainties in the experiments.

4. Results and discussion

4.1. Primary nozzle performance

The performance of the primary nozzle was evaluated by recording its mass flow rate, pressure, and temperature using a Lab View data acquisition system. The pressure was measured at the last point in the primary line before it entered the ejector and well downstream of the flow meter's location. The correlation between primary pressure and flow rate was established for each nozzle throat separation and is depicted in Fig. 8. The data points are well within 1 % error for each nozzle throat separation. The correlation is defined by the three equations included in Fig. 8. This correlation is assumed to remain valid even after removing the flow meter from the line, since the geometry downstream of the primary pressure transducer remains unchanged. This means that the primary mass flow rate can be related to the primary pressure through the established correlation, even when the flow meter

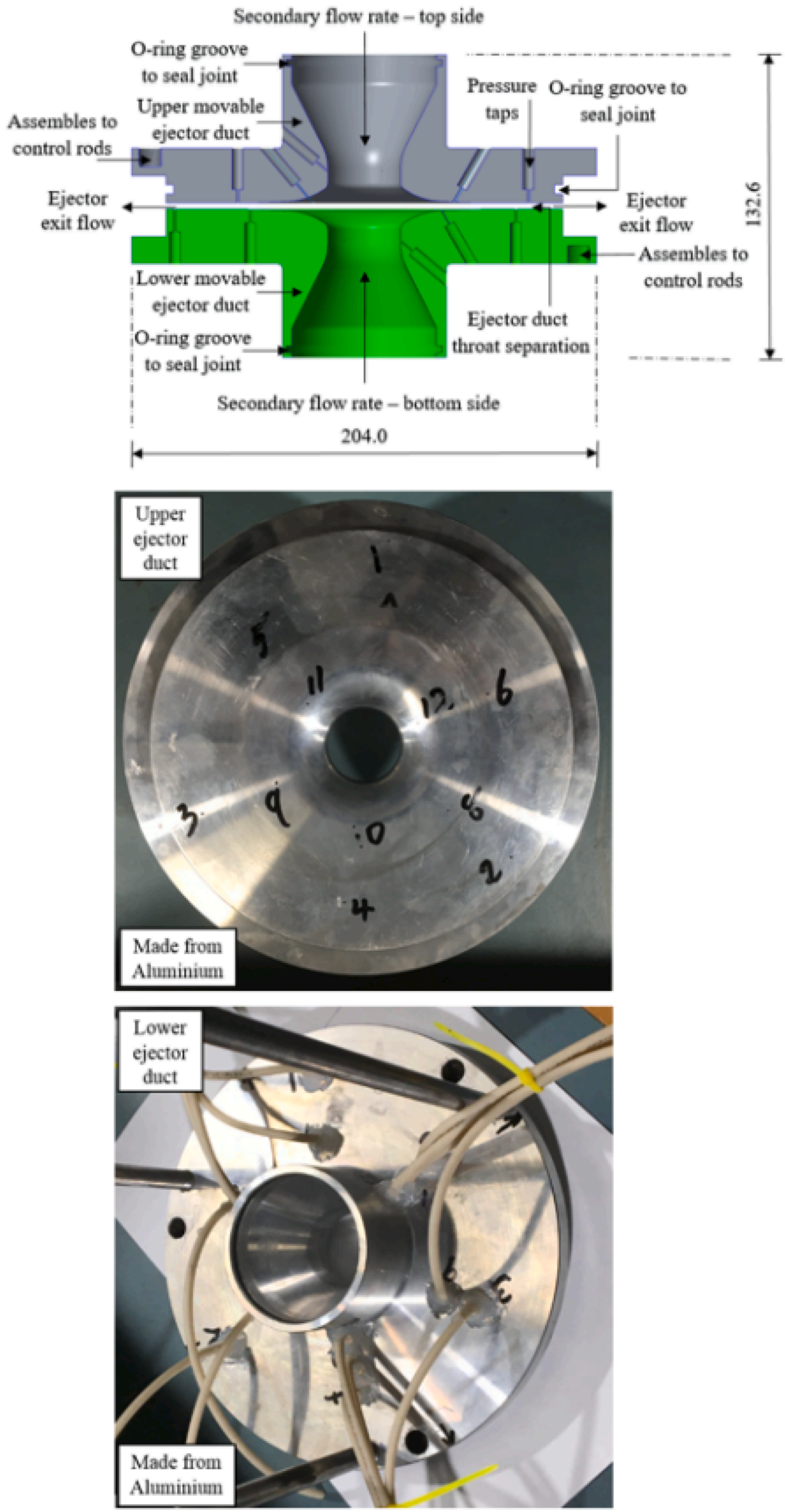

Fig. 6. The image depicts a cross-sectional schematic and real-life images of the variable radial ejector ducts, with all measurements in millimetres.

Table 2
Geometric parameters of the original VGRE and the improved VGRE.

Characteristic	Original VGRE	Improved VGRE (Variable geometry)
Nozzle throat separation (mm)	0.5	0.4, 0.5, 0.6
Nozzle throat area (mm^2)	11.0	8.8, 11.0, 13.2
Nozzle exit area (mm^2)	180	171, 180, 188
Nozzle area ratio	16.4	19.4, 16.4, 14.2
Nozzle divergent half angle (degree)	5.0°	5.0°
Divergent nozzle length (mm)	9.5	9.5
Diameter of nozzle disc (mm)	26	26
Mixing chamber length (mm)	20	35
Duct throat separation (mm)	2.3	2.3, 2.6, 3.0
Duct throat area (mm^2)	520	737, 833, 961
Diffuser exit area (mm^2)	1040	1257, 1421, 1639
Diffuser length (mm)	36	36
Diffuser area ratio	2.0	1.7
Ejector area ratio	47	56, 63, 67, 73, 76, 84, 87, 95, 109
Ejector divergent half angle (degree)	0.0°	0.0°
Ejector flow path length (mm)	72	87
Diameter of ejector duct disc (mm)	144	174

Table 3
Measurement technique details.

Sensor	Range	Accuracy
Pressure transducers (Wika model A-10)	High range is 0–6 bar, low range is 0 to −1 bar	0.5 %
Thermocouples (K-type)	0–250 °C	0.7 %
Flowmeter device (FMA-2600A-OMEGA)	0–5 g/s	0.8 %

is no longer present in the primary line. After establishing the correlation between primary flow rate and primary pressure, the flow meter was attached to the secondary flow line.

Fig. 9 shows the results of the primary flow rate for different nozzle throat separations and primary pressures ranging from 160 kPa to 300 kPa. The results indicate that an increase in nozzle throat separation led to an increase in the primary flow rate for each pressure due to an increase in nozzle throat area. For example, with a primary pressure of 250 kPa, the primary flow rate increased by 49 % when the nozzle throat separation was changed from 0.4 mm to 0.6 mm. The primary flow rate also increased with an increase in primary pressure for each nozzle throat separation. When the primary pressure increased from 160 kPa to 300 kPa, the primary flow rate increased by 88 % for a nozzle throat separation of 0.5 mm, which aligns with the principle that mass flow through an orifice is proportional to the orifice's cross-sectional area and the supply pressure. The discharge coefficient (C_d) was approximately 0.92 for each operating condition and nozzle throat separation. The VGRE was improved with manual adjustment mechanisms to change the primary nozzle throat separation during the experiments, and the uncertainty in achieving the target nozzle throat separations of 0.4, 0.5, and 0.6 mm was estimated to be ±8 %, which includes the estimated uncertainties in nozzle throat separations of 0.4 ± 0.03, 0.5 ± 0.04, and 0.6 ± 0.05 mm.

4.1.1. Symmetry of flow between ejector duct plates

The secondary flow enters the ejector duct plates from the upper and lower secondary flow lines. To measure the flow rate and compare the flow in both lines, an orifice was placed in each secondary flow line. Although the ejector duct plates were assembled inside the receiving tank, it was not possible to observe the flow between them. Fig. 10 displays the differential pressure across the orifice plates under different operating conditions. The pressure drops across the orifice plate remained consistent between the upper and lower secondary flow lines for each geometry, with a maximum deviation of 0.032 kPa. The maximum difference in secondary flow rate between the upper and lower secondary flow lines was about 3.5 % (based on the 7.5 % maximum deviation in pressure drop). The uncertainty in the duct throat separation was estimated at around ±7.5 %, with the estimated duct throat separation being 2.3 ± 0.2, 2.6 ± 0.2 and 3.0 ± 0.2 mm. These uncertainties were low enough to permit meaningful comparison of the three cases. The results showed that the lower flow line consistently had a higher pressure drop. This difference could be attributed to the primary line in the upper secondary pipe, which altered the secondary flow paths in the experimental setup.

4.2. Performance curve analysis

To assess the performance of the improved VGRE, experiments were conducted using primary pressures of 160, 200, 250, 270, and 300 kPa, and secondary pressures of 1.2, 1.5, and 1.8 kPa, resulting in critical outlet pressures from 2.4 kPa to 8.0 kPa. The nozzle throat separations of 0.4, 0.5, and 0.6 mm and duct throat separations of 2.3, 2.6, and 3.0 mm were evaluated, covering a range of nozzle and ejector area ratios from 14.2 to 19.4 and 56 to 109, respectively.

Fig. 11 displays the performance of the improved VGRE at a primary pressure of 250 kPa and a secondary pressure of 1.8 kPa, with a nozzle throat separation of 0.4 mm and a duct throat separation of 3.0 mm. A horizontal line representing the maximum entrainment ratio is shown for the choked flow region. If the difference between the maximum entrainment ratio and the entrainment ratio exceeds 2 %, the outlet pressure at that entrainment ratio is identified as P_o^*, which was 3.94 kPa in this case. The improved VGRE showed similar behaviour to conventional axial flow ejectors, operating in the choked flow region (on-design condition) where the entrainment ratio remained constant at a lower outlet pressure than the critical outlet pressure (P_o^*). In this region, both primary and secondary flows were choked, resulting in an entrainment ratio that was not dependent on downstream conditions. The critical outlet pressure was the highest pressure at which the highest entrainment ratio could be maintained. Beyond the critical outlet pressure, the improved VGRE entered the unchoked flow region (off-design condition), with the secondary flow unchoked and the primary flow still choked. The entrainment ratio decreased as the outlet pressure increased and reached zero at the malfunction pressure. Any increase beyond the malfunction pressure would cause a reverse flow into the secondary flow inlet, causing the ejector to stop functioning as a compressor.

The experimental data for the entrainment ratio, such as presented in Fig. 11 was used to determine the critical outlet pressure for each operating condition. This was achieved by fitting a horizontal line to the experimental results in the choked flow region, resulting in an entrainment ratio of not less than 0.98 of the maximum entrainment ratio for each experiment at the critical outlet pressure. Beyond the critical outlet pressure, in the unchoked flow region, the entrainment ratio declined gradually in generally two linear stages. The first stage had a lower rate of reduction in entrainment ratio, while the second stage had an increased rate of reduction, typically starting halfway between the critical outlet pressure and the malfunction pressure. The method for calculating the entrainment ratio and critical outlet pressure was consistent for all the experimental data.

Note that in all cases, a large number of data points were obtained across the range of P_o values. For example, in Fig. 11, the experimental data line actually consists of 8700 individual data points for $2.63 < P_o$ less than 4.58 kPa.

4.3. Primary and secondary pressure effects

The impact of primary and secondary flow pressures on ejector

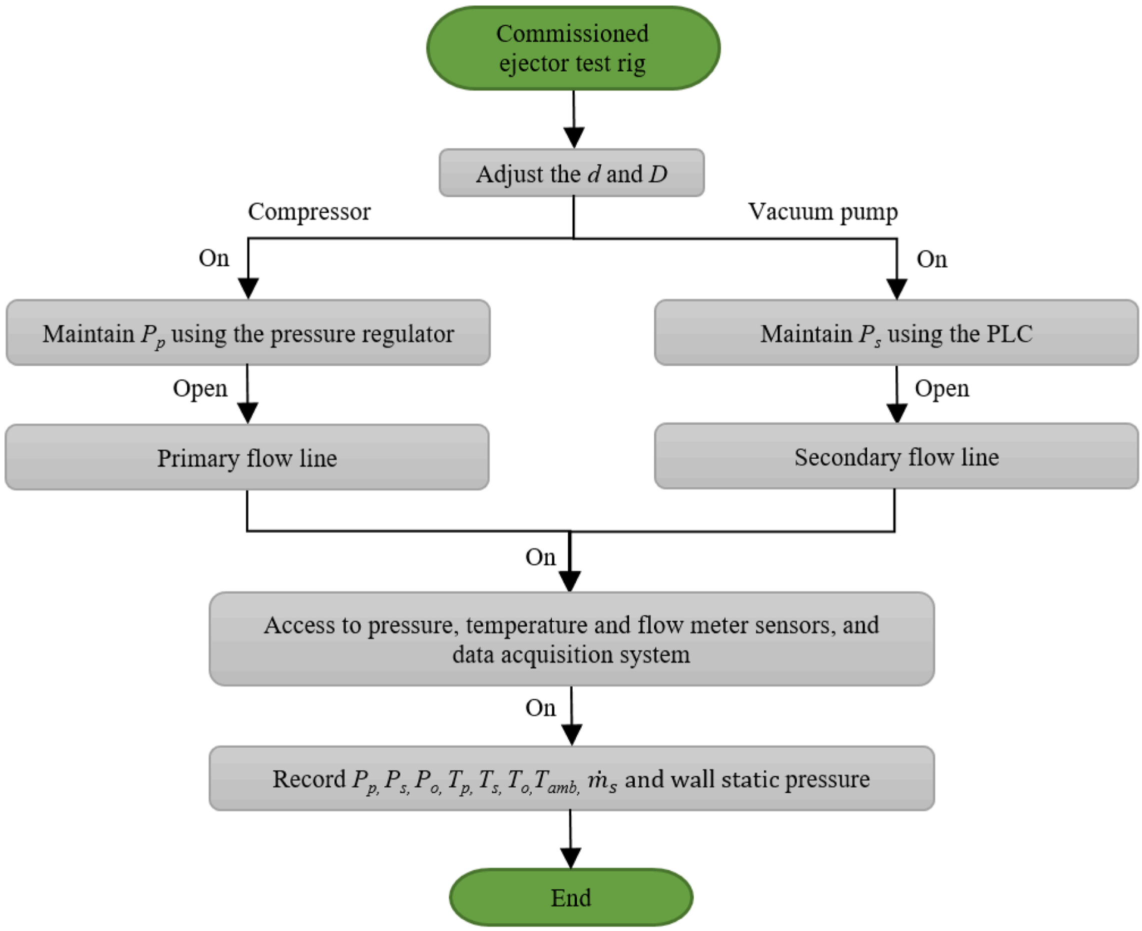

Fig. 7. Flowchart outlining the experimental procedure.

Table 4
Geometrical parameters and operating conditions in the experiments.

Geometrical parameters	Operating conditions
Nozzle throat separation (d) = 0.4, 0.5, and 0.6 mm Duct throat separation (D) = 2.3, 2.6 and 3.0 mm Ejector area ratio (AR) = 56, 63, 67, 73, 76, 84, 87, 95, and 109	Pp = 160, 200, 250, 270, and 300 kPa Ps = 1.2, 1.5, and 1.8 kPa

performance was studied and the results are displayed in Fig. 12 to Fig. 15. These findings broadly align with previous research results on variable geometry axial ejectors [45–51]. Fig. 12 depicts the effect of varying primary pressures (160, 200 and 270 kPa) with a constant secondary pressure of 1.8 kPa, using fixed nozzle and duct throat separations of 0.5 mm and 2.6 mm, respectively. Results showed that the entrainment ratio increases as primary pressure decreases, but critical outlet pressure decreases. A decrease in primary pressure from 270 kPa to 160 kPa resulted in a 91 % increase in entrainment ratio but a 38 % decrease in critical outlet pressure.

Fig. 13 shows the effect of varying primary pressures on ejector

Table 5
Experimental performance of the improved VGRE with different nozzle and duct throat separations for a nominal primary pressure of 200 kPa and a nominal secondary pressure of 1.8 kPa.

	Run 1	Run 2	Run 3	Run 4	Run 5	Run 6	Run 7	Run 8	Run 9
d in mm	0.4	0.4	0.4	0.5	0.5	0.5	0.6	0.6	0.6
D in mm	2.3	2.6	3.0	2.3	2.6	3.0	2.3	2.6	3.0
AR	84	95	109	67	76	87	56	63	73
AR_n	19.4	19.4	19.4	16.4	16.4	16.4	14.2	14.2	14.2
P_{atm} in kPa	93.92	94.11	93.55	94.50	94.64	94.03	94.17	94.76	94.43
T_{amb} in °C	24.6	23.7	22.3	18.1	21.8	26.0	23.7	20.3	24.0
T_p in °C	25.2	24.3	22.5	18.1	22.0	26.4	24.2	20.6	23.6
T_s in °C	26.7	26.0	24.2	19.7	24.1	28.6	26.7	22.8	25.8
T_o in °C	25.5	24.5	23.2	18.9	22.1	26.8	24.2	20.8	24.7
P_p in kPa	200.33	199.73	202.71	202.20	201.63	198.67	200.10	199.44	199.97
P_s in kPa	1.80	1.81	1.81	1.82	1.79	1.81	1.83	1.80	1.81
$\dot{m}_s$ in g/s	3.03	3.40	4.01	2.91	3.11	3.73	2.85	3.26	3.60
$\dot{m}_p$ in g/s	3.80	3.80	3.80	4.75	4.75	4.75	5.67	5.67	5.67
P_o* in kPa	3.06	3.50	3.36	5.00	4.76	4.30	5.33	5.32	4.86
ω	0.80	0.89	1.06	0.61	0.65	0.79	0.50	0.57	0.63

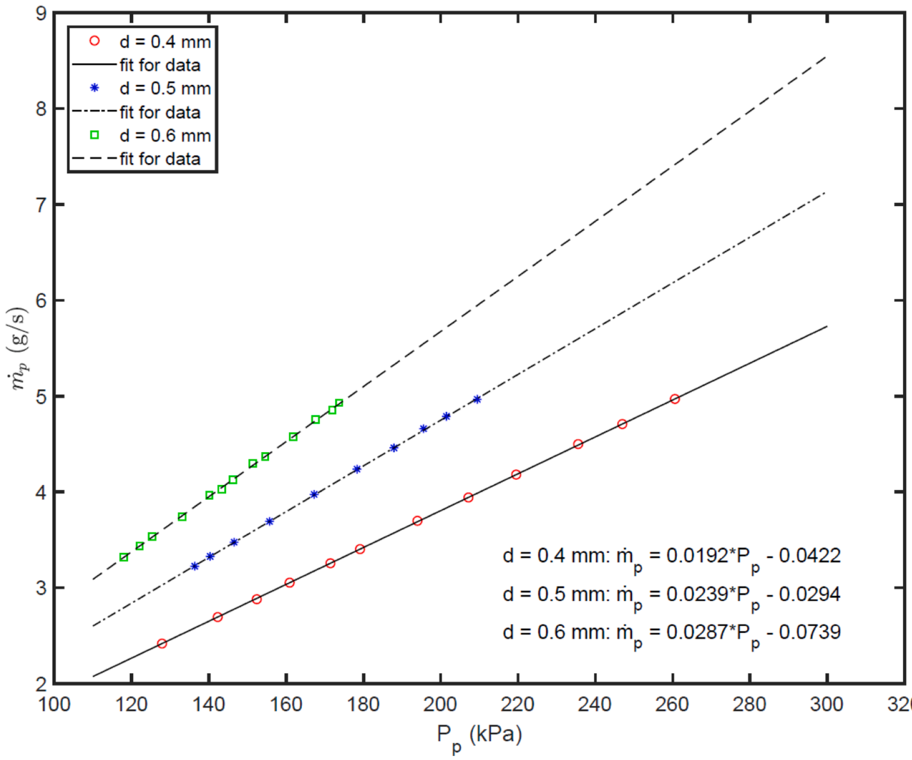

Fig. 8. Relationship between primary pressure and mass flow rate at different nozzle throat separations (0.4, 0.5, and 0.6 mm).

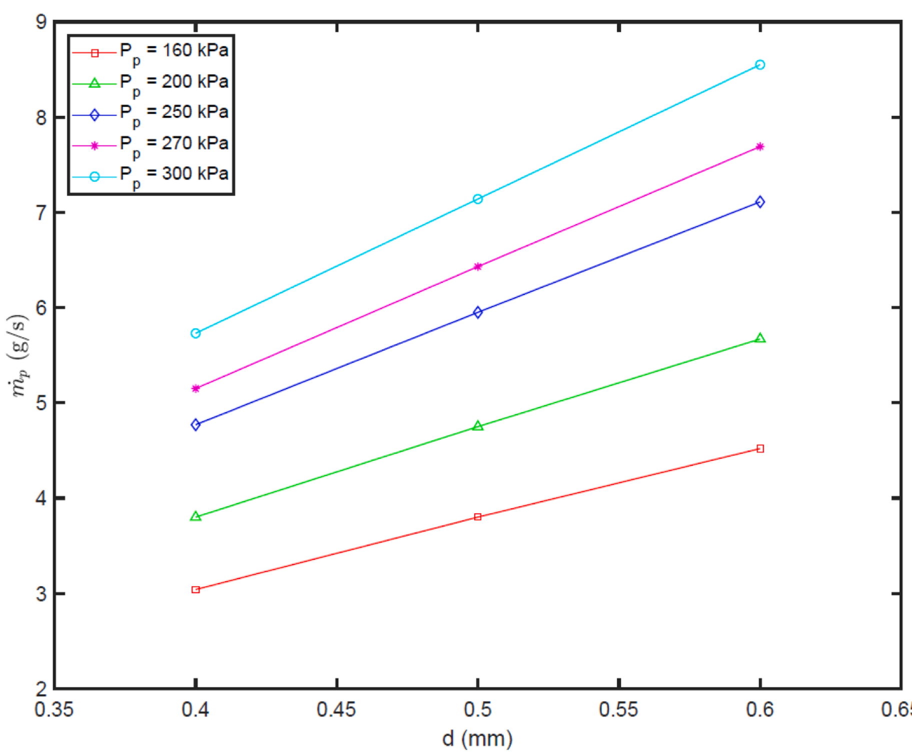

Fig. 9. Primary flow rate as function of nozzle throat separation for different primary pressures.

performance (entrainment ratio and critical outlet pressure) with a constant secondary pressure of 1.8 kPa and fixed nozzle and duct throat separations of 0.5 mm and 2.6 mm. An increase in primary pressure leads to an under-expanded primary jet exiting the nozzle, reducing the effective entrainment area for the secondary stream. This decreases the secondary flow rate while increasing the primary flow rate. The result is a reduction in entrainment ratio and an increase in critical outlet pressure due to the increased momentum of the mixed stream. These results indicate that higher primary pressure leads to a decrease in entrainment ratio and an increase in critical outlet pressure.

Fig. 14 illustrates the impact of different secondary pressures (1.2, 1.5, and 1.8 kPa) on the ejector performance, with a constant primary

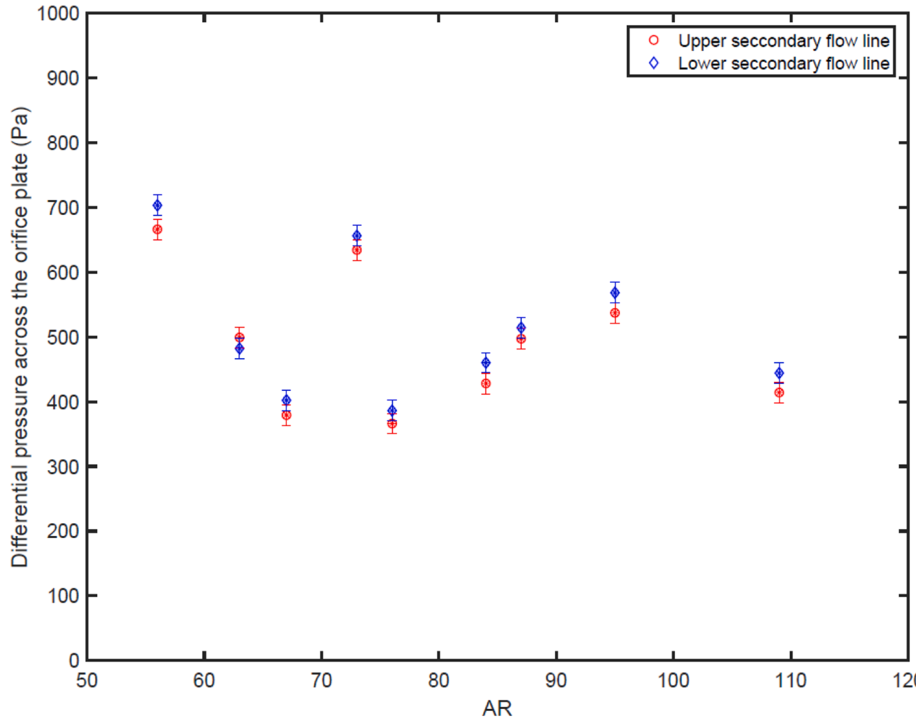

Fig. 10. Differential pressure across the orifice plates measuring the secondary flow rate for different ejector area ratios.

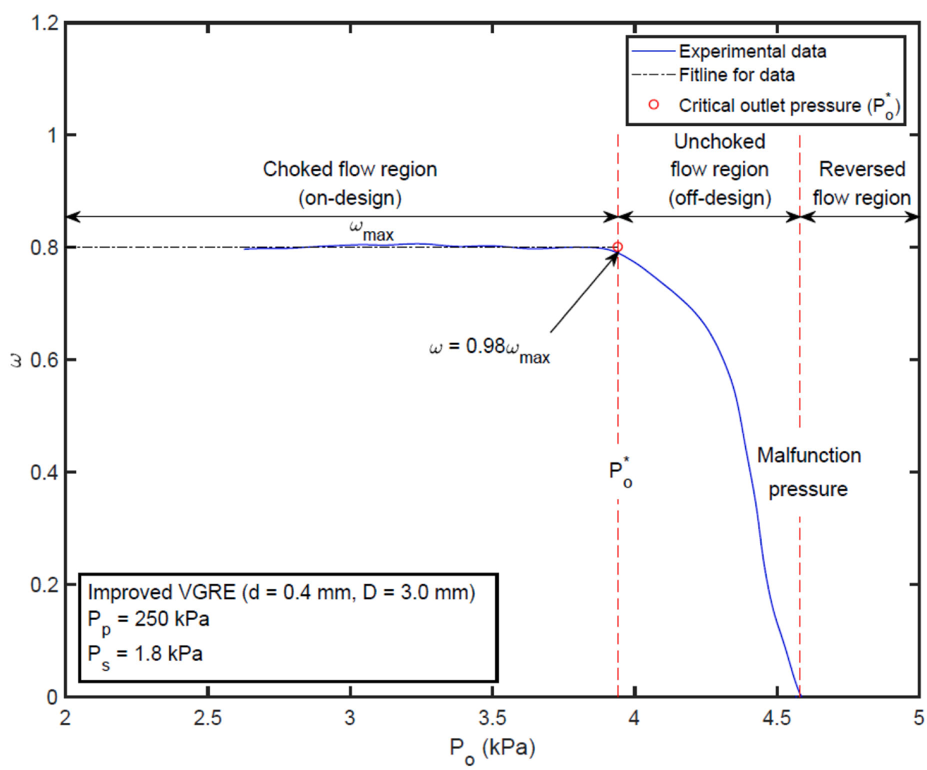

Fig. 11. Entrainment ratio variation with outlet pressure for primary pressure of 250 kPa and secondary pressure of 1.8 kPa for nozzle throat separation of 0.4 mm and duct throat separation of 3.0 mm.

pressure of 200 kPa and fixed nozzle and duct throat separations of 0.5 mm and 2.6 mm, respectively. The results showed that both the entrainment ratio and critical outlet pressure increased as the secondary pressure rose. The entrainment ratio increased by about 65 % when the secondary pressure went from 1.2 kPa to 1.8 kPa, while the critical outlet pressure rose by around 12 %.

Fig. 15 shows the effect of secondary pressure on the ejector's performance, with a constant primary pressure of 200 kPa. The results indicated that a higher secondary pressure increases the effective area for entrainment of the secondary stream, and thus the entrainment ratio and critical outlet pressure. Similar trends have been previously reported in axial ejector studies [50–55].

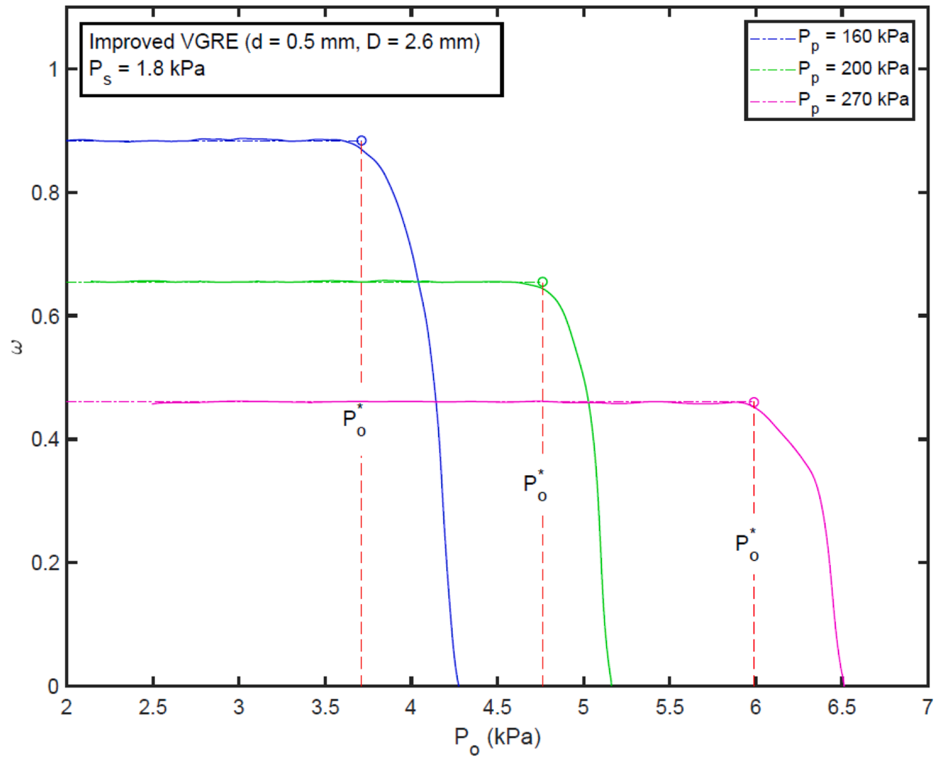

Fig. 12. Entrainment ratio variation with outlet pressure at primary pressures 160, 200 and 270 kPa.

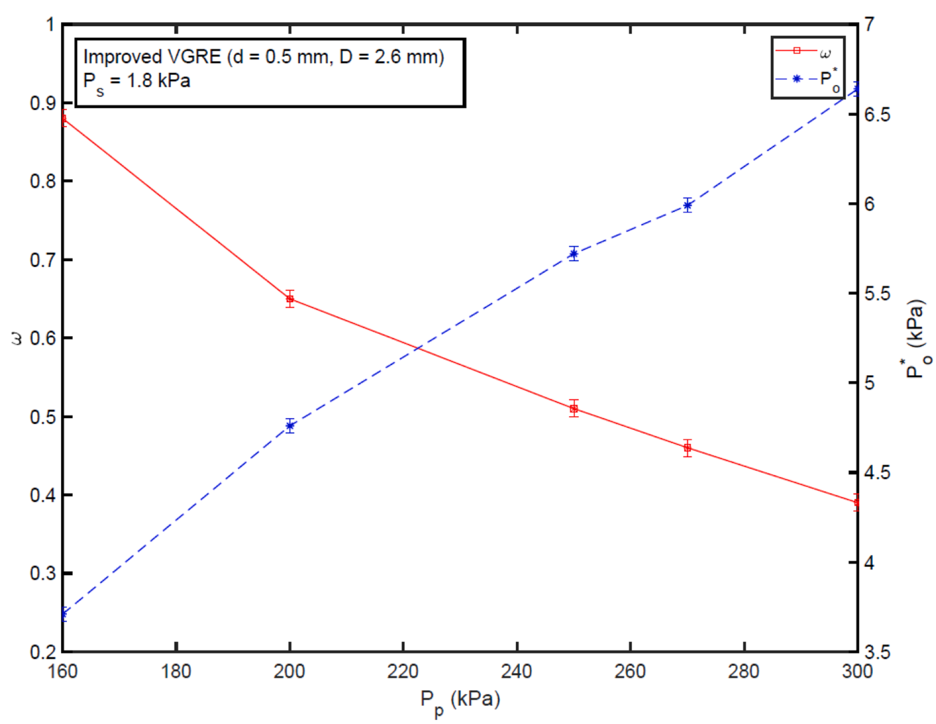

Fig. 13. Entrainment ratio and critical outlet pressure variation with primary pressure.

4.4. Nozzle throat separation effect

The study of the effect of nozzle throat separation on the performance of the improved VGRE was conducted for duct throat separations of 2.3 mm, 2.6 mm, and 3.0 mm, as shown in Fig. 16. The results were obtained with a primary pressure of 250 kPa and a secondary pressure of 1.8 kPa. The entrainment ratio is represented by solid lines and the critical outlet pressure by dashed lines. The results indicated that the maximum entrainment ratio was achieved when the ejector had a small nozzle throat separation and a large duct throat separation. For example, with a large nozzle throat separation of 0.6 mm, the improved VGRE had a minimum entrainment ratio of 0.41 when the duct throat separation was 2.6 mm. However, by reducing the nozzle throat separation to 0.4 mm, the entrainment ratio improved to 0.69, a 68 % increase. Similar

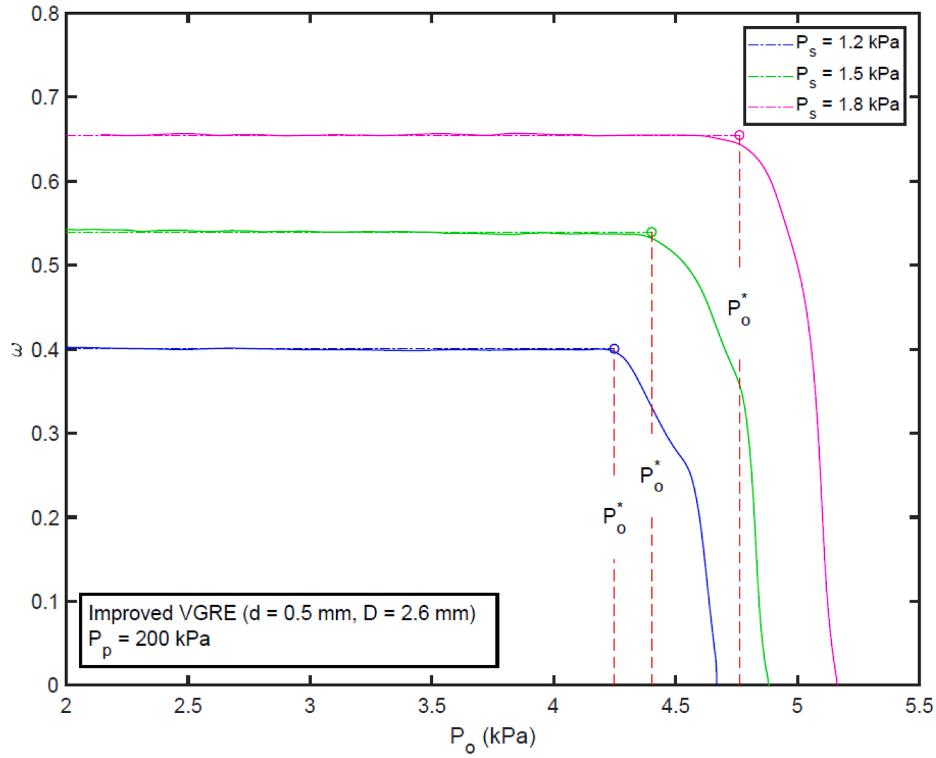

Fig. 14. Entrainment ratio variation with outlet pressure at secondary pressures 1.2, 1.5 and 1.8 kPa.

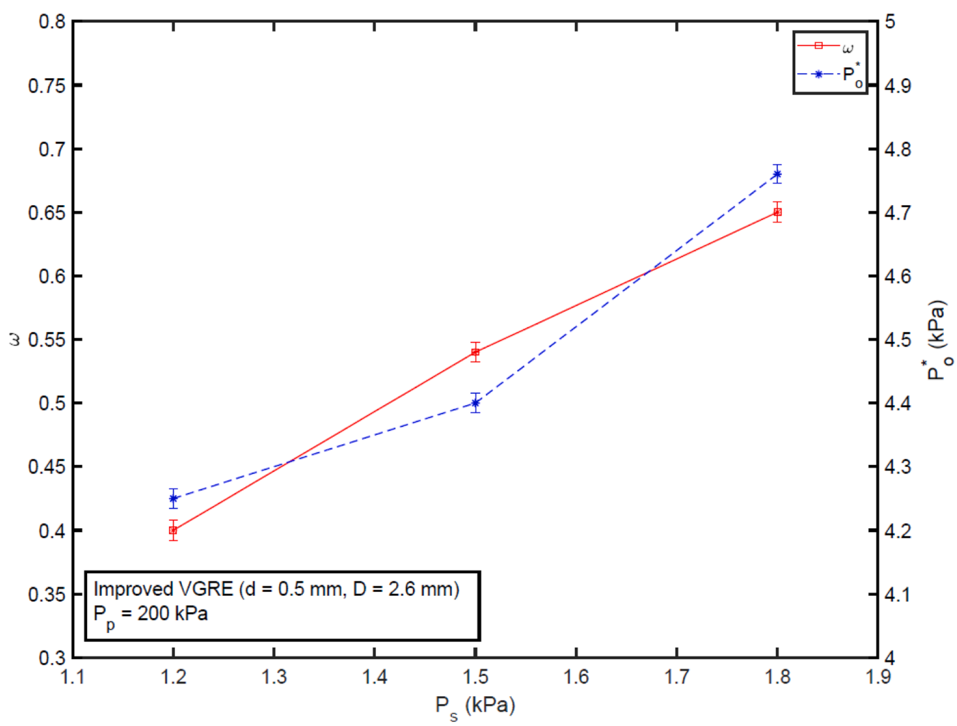

Fig. 15. Entrainment ratio and critical outlet pressure variation with secondary pressure.

observations were made for the other duct throat separations.

The improved VGRE could operate with any nozzle throat separation between 0.4 mm and 0.6 mm, and a wider range of nozzle separations may be possible for different operating conditions and geometries. On the other hand, the maximum critical outlet pressure was achieved when the ejector had a large nozzle throat separation and a small duct throat separation. For example, with a small nozzle throat separation of 0.4 mm, the improved VGRE had a minimum critical outlet pressure of 4.13 kPa when the duct throat separation was 2.6 mm. But by increasing the nozzle throat separation to 0.6 mm, the critical outlet pressure increased to 6.35 kPa, a 54 % improvement. Similar observations were made for the other duct throat separations, indicating that the improved VGRE could operate with a nozzle throat separation larger than 0.6 mm for a higher critical outlet pressure but a lower entrainment ratio.

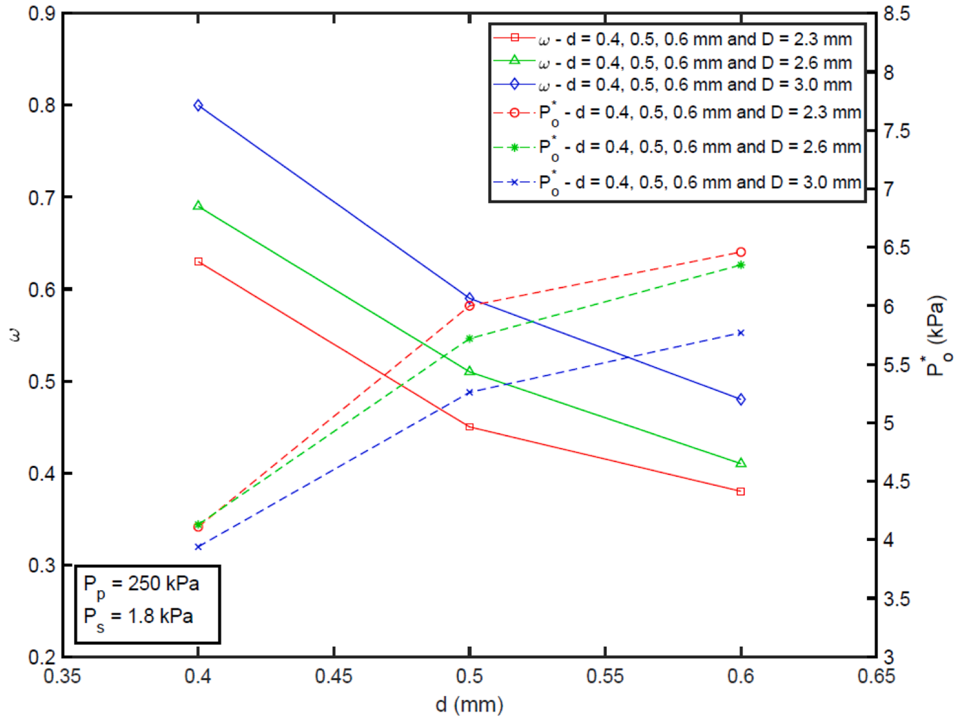

Fig. 16. Entrainment ratio and critical outlet pressure variation with nozzle throat separation.

The variation in nozzle and ejector throat areas affects the entrainment ratio and critical outlet pressure. The entrainment ratio is linked to the available flow area, while the critical outlet pressure is linked to the relative momentum flux. An increase in nozzle throat separation leads to a rise in the momentum flux of the primary stream compared to the secondary stream. The rise in primary mass flow rate reduces the available flow area for the secondary stream when the duct throat separation is constant, leading to a higher critical outlet pressure but lower entrainment ratio.

4.5. Duct throat separation effect

The impact of duct throat separation on the performance of the improved VGRE was studied for three nozzle throat separations (0.4 mm, 0.5 mm, and 0.6 mm) and the results are displayed in Fig. 17. The experiments were conducted with a primary pressure of 250 kPa and a secondary pressure of 1.8 kPa. The entrainment ratio is presented with solid lines and the critical outlet pressure is shown as dashed lines. The highest entrainment ratio was achieved with a large duct throat

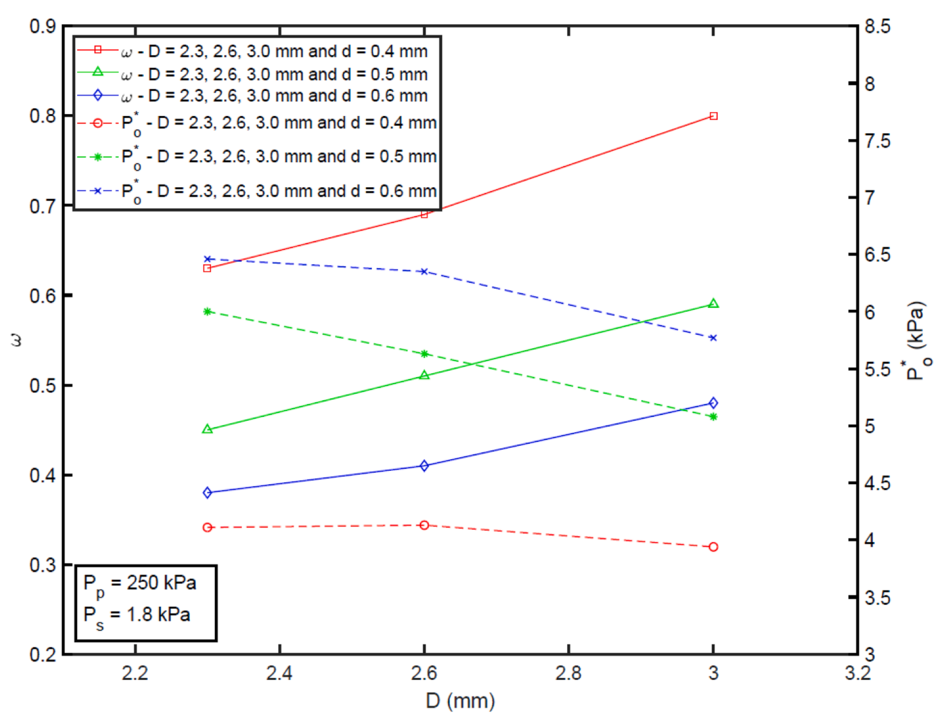

Fig. 17. Entrainment ratio and critical outlet pressure variation with duct throat separation.

separation and a small nozzle throat separation. For example, with a nozzle throat separation of 0.6 mm, the improved VGRE had a minimum entrainment ratio of 0.38 when the duct throat separation was 2.3 mm. By increasing the duct throat separation to 3.0 mm, the entrainment ratio improved to 0.48, a performance improvement of about 26 %. Similar trends were observed for the other nozzle throat separations.

The improved VGRE was found to operate effectively with duct throat separations ranging from 2.3 mm to 3.0 mm. Other operating conditions and geometries may permit a wider range of duct separations. The variations in the critical outlet pressure curves can be attributed to the possible differences in the flow asymmetry between the ejector duct plates at different separations. In narrow ducts, the asymmetry might be restricted, while wider ducts provide space on either side of the primary jet, reducing asymmetry in the flow. The combination of a 0.5 mm primary duct separation and the narrowest duct separation may lead to the most significant interference in the secondary flow due to potential asymmetry. The highest critical outlet pressure was achieved when the ejector operated with a small duct throat separation and a large nozzle throat separation. For example, with a duct throat separation of 3.0 mm, the improved VGRE had a minimum critical outlet pressure of 5.77 kPa for a nozzle throat separation of 0.6 mm, which increased to 6.46 kPa when the duct throat separation was reduced to 2.3 mm, representing a 12 % performance improvement. At small nozzle throat separations (e.g. 0.4 mm), the critical outlet pressure remained constant for different duct throat separations. This is likely due to an increase in flow asymmetry between the ejector duct plates at different separations, leading to a constant critical outlet pressure.

With increasing duct throat separations, the ejector area ratio increases for each nozzle throat separation. This occurs because the available flow area for the secondary flow increases, while the primary mass flow rate remains constant due to the choked nozzle. This allows for a change in the secondary flow rate in both on-design and off-design operations by adjusting the duct throat separation. However, increasing the duct separation leads to a higher entrainment ratio, but a lower critical outlet pressure.

4.6. Expansion ratio effect

The impact of area ratio on the performance of the improved VGRE was examined for different area ratios that result from adjusting nozzle and duct throat separations. Fig. 18 and Fig. 19 demonstrate that the improved VGRE achieved entrainment ratios ranging from 1.26 to 0.29 and critical compression ratios from 1.35 to 4.43, respectively, for expansion ratios between 89 and 167 and ejector area ratios between 56 and 109. It's important to note that the high expansion ratio of 167 was achieved through two operating conditions: 200 kPa primary pressure and 1.2 kPa secondary pressure, and 300 kPa primary pressure and 1.8 kPa secondary pressure.

The relationship between expansion ratio and entrainment ratio for the improved VGRE with various ejector area ratios is shown in Fig. 18. The highest entrainment ratio was reached when the ejector operates with a low expansion ratio and high ejector area ratio. According to the experimental data, low expansion ratios correspond to high entrainment ratios and vice versa, regardless of the ejector area ratio. The maximum change in entrainment ratio for a fixed geometry ejector with an area ratio of 87 was 136 % when the expansion ratio decreased from 167 to 89. In contrast, the improved VGRE had a maximum change in entrainment ratio of 334 % when the expansion ratio decreased from 167 to 89 and the ejector area ratio increased from 56 to 109. The average improvement in entrainment ratio for the improved VGRE across all area ratios and operating conditions was 146 %. This confirms that entrainment ratio varies inversely with expansion ratio in a fixed geometry ejector optimized for high performance. Similar results were reported by several researchers for variable geometry axial ejectors [56–58]. To summarize, increasing the area ratio is necessary for optimal entrainment performance when expansion ratio increases during operation.

The influence of expansion ratio on critical compression ratio for varying ejector area ratios is shown in Fig. 19. The highest critical compression ratio was reached when the ejector operates with a high expansion ratio and low ejector area ratio. According to the experimental data, high expansion ratios correspond to high critical

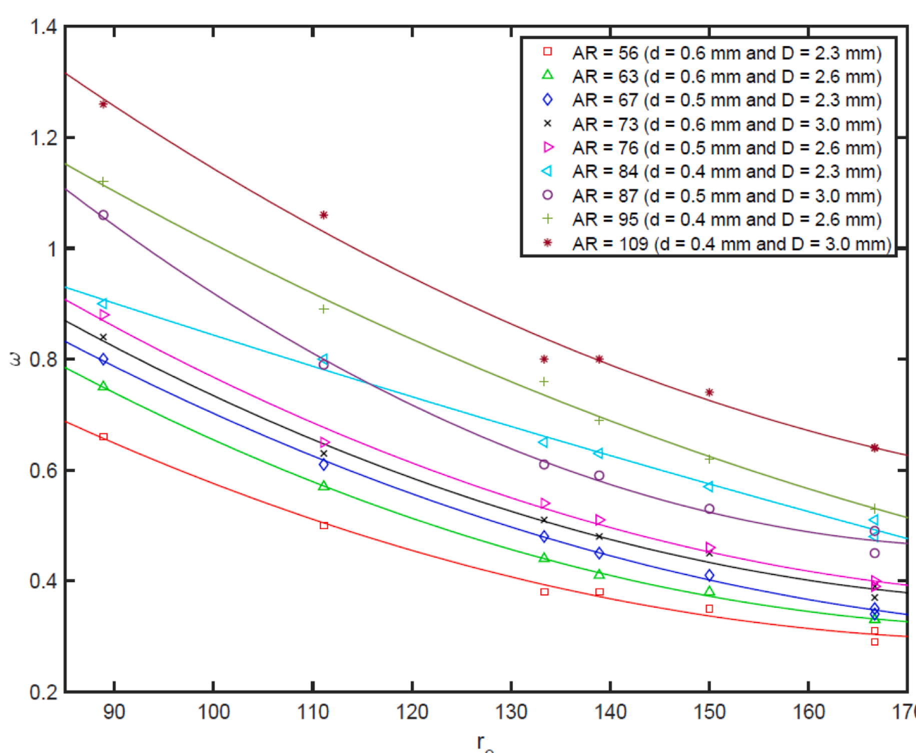

Fig. 18. Experimental results of entrainment ratio as a function of the expansion ratio for different ejector area ratios.

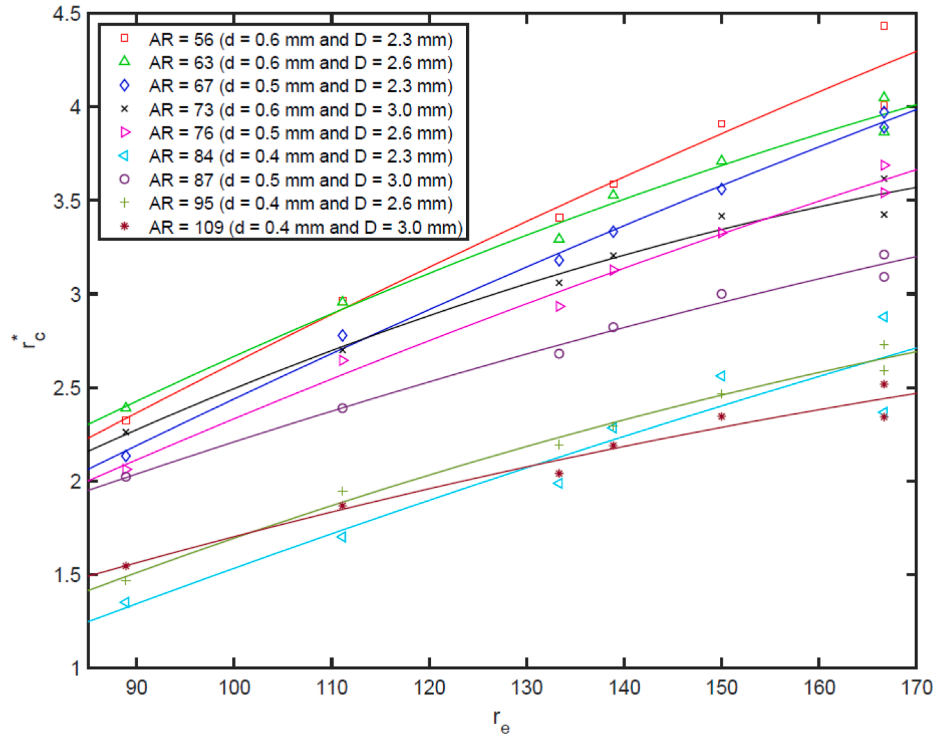

Fig. 19. Experimental results of critical compression ratio as a function of the expansion ratio for different ejector area ratios.

compression ratios and vice versa, independent of the ejector area ratio. The maximum change in critical compression ratio for a fixed geometry ejector with an area ratio of 84 was 113 % when the expansion ratio increased from 89 to 167. Conversely, the improved VGRE had a maximum change in critical compression ratio of 226 % when the expansion ratio increased from 89 to 167 and the ejector area ratio decreased from 84 to 56. The average improvement in critical compression ratio for the improved VGRE across all area ratios and operating conditions was 100 %. This confirms that critical compression ratio varies with expansion ratio in a fixed geometry ejector optimized for high performance. Similar results were reported by several researchers for variable geometry axial ejectors [50,57,59]. In conclusion, decreasing the area ratio is necessary for optimal performance in critical compression ratio when expansion ratio decreases due to variations in

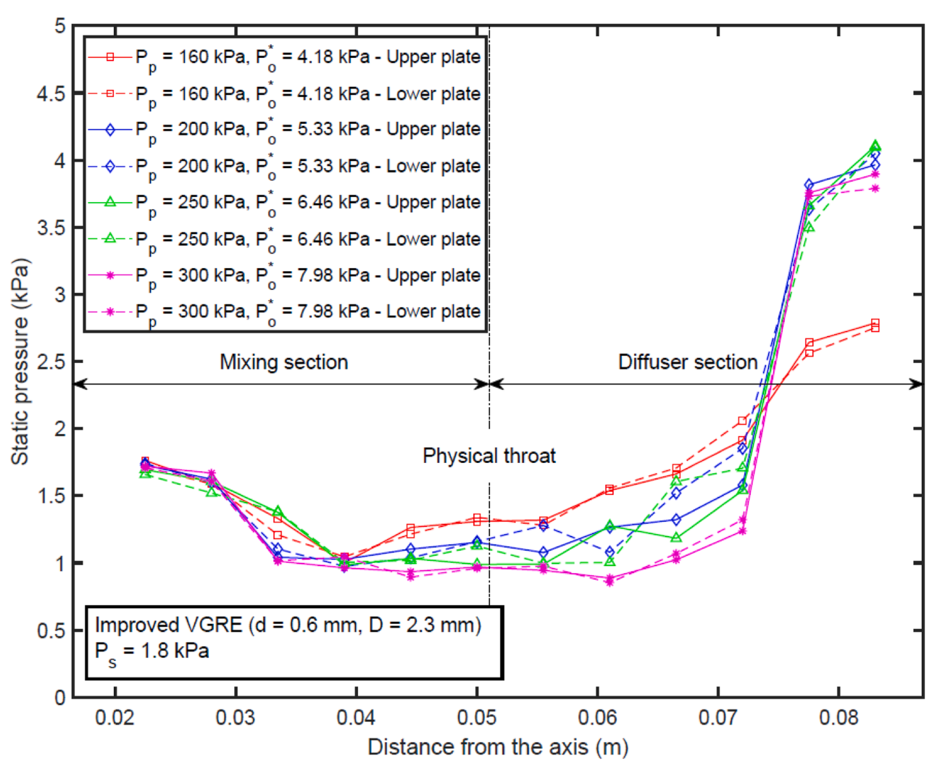

Fig. 20. Static pressure on the walls of the ejector duct for various primary pressures for the improved VGRE operating at critical outlet pressure.

operating conditions like solar insolation and outdoor temperature, and vice versa.

4.7. Wall static pressure

The variation in static pressure along the walls of both upper and lower ejector duct plates was measured for each condition. Fig. 20 displays the distribution of static pressure along the ejector wall for a range of primary pressures (1.8 kPa secondary pressure) and nozzle/duct throat separations of 0.6 mm and 2.3 mm respectively. The results showed consistency between the upper and lower plates for each experiment's static pressure distribution. The solid lines in the figure represent the results for the upper ejector duct plate and the dash lines represent the results for the lower ejector duct plate. The physical throat of the ejector is also marked in the figure.

To obtain the wall pressure data with sufficient accuracy, six low-pressure transducers were installed in the mixing section and six were installed in the diffuser section for each ejector duct plate. The static pressure curves started at approximately the same pressure as the secondary pressure and then decreased in the mixing section to reach a minimum at 39 mm from the ejector axis. The static pressure varied inversely with the primary pressure on each side of the duct throat, but all the curves showed the same trend. The lowest wall pressures were found to occur between 39 and 61 mm from the ejector axis and could be located upstream or downstream of the physical throat.

Fig. 21 displays the static pressure distribution along the ejector wall for a range of secondary pressures (200 kPa primary pressure) and nozzle/duct throat separations of 0.6 mm and 2.3 mm respectively. The results showed consistency between the upper and lower plates for each operating condition. At 72 mm from the ejector axis in the diffuser section, the static pressures rapidly increased near the duct exit, indicating a final deceleration of the flow before it enters the receiving tank. All the static pressure curves showed approximately the same trend. The local wall pressure at the physical throat was related to the secondary pressure for constant primary pressure, and increasing the secondary pressure resulted in a slight increase in the wall static pressure at the measured position. The lowest wall pressures were also found to occur between 39 and 61 mm from the ejector axis and could be located upstream or downstream of the physical throat.

5. Gas dynamic model

5.1. Comparison with a gas dynamic model

The performance evaluation of different types of axial ejectors was conducted using a one-dimensional gas dynamic model, initially introduced by Buttsworth [60]. This model enabled the prediction of entrainment ratios and critical compression ratios of the ejectors, as well as the determination of calibration factors suitable for different ejector types. In this particular study, the improved VGRE was subjected to the model to estimate its entrainment and critical compression ratios across various expansion and ejector area ratios. Subsequently, the simulation results obtained from the one-dimensional gas dynamic model for the improved VGRE were compared to experimental data.

The gas dynamics model [60] applies the compressible flow equations for mass, momentum, and energy conservation to the primary, secondary, and mixed streams. Notably, this model did not consider friction and heat transfer effects between the fluid and ejector walls, and it did not incorporate isentropic and discharge coefficients commonly used in other ejector models. Complete mixing within the mixing chamber was assumed. For a comprehensive description of this model, interested readers are advised to refer to [60]. In the present application for the simulation of the VGRE, mixing was handled using the constant area equations, with a specific value ranging from 737 to 961 mm^2 specified for this area depending on the separation of the duct plates. The model assumed that the static pressures of the primary and secondary streams were matched at the entry to the mixing chamber. The maximum achievable Mach number in the secondary stream at the entrance to the mixing chamber was unity, which corresponded to conditions of maximum entrainment ratio. Critical compression ratio conditions were attained when a normal shock was positioned at the exit of the mixing chamber.

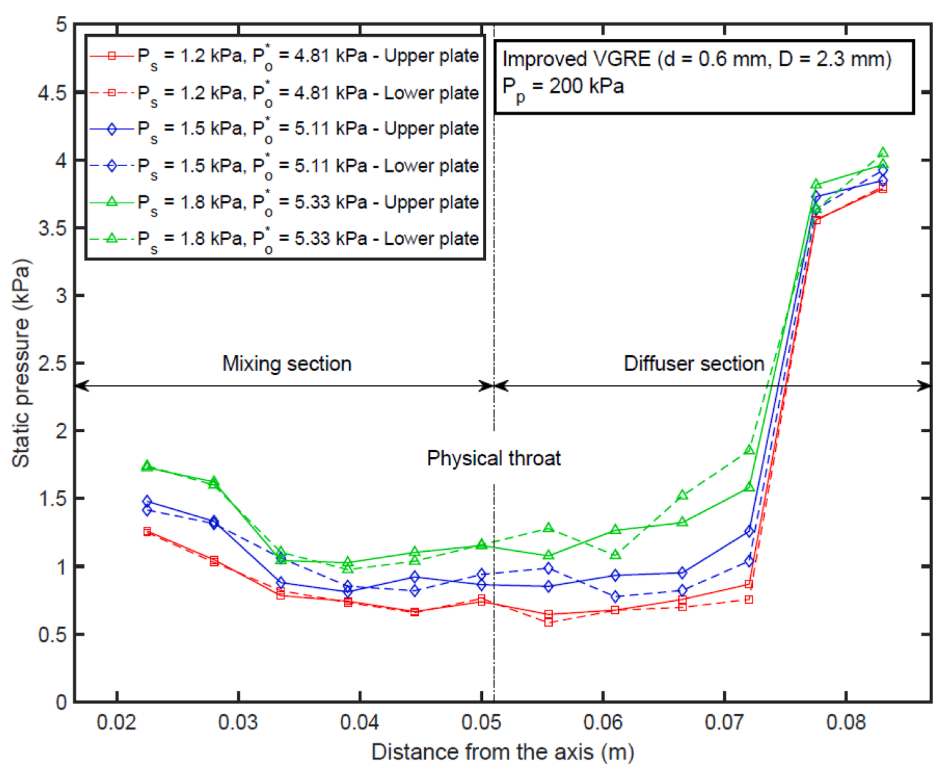

Fig. 21. Static pressure on the walls of the ejector duct for various secondary pressures for the improved VGRE operating at critical outlet pressure.

It is worth noting that the model consistently overestimated the critical compression ratio when compared to experimental results obtained for various axial ejectors, expansion ratios, and working fluids. To address this discrepancy, an adjustment to the values from the model was calculated according to the correlation described in [60], as:

$$\Delta r_c^* = -4.61*10^{-3} r_e - 0.397 \tag{5}$$

where Δr_c^* is the critical compression ratio. The one-dimensional Gas Dynamic Model (GDM) had a representative uncertainty of around ± 20 %, according to Buttsworth [60]. After applying the experimental value of the expansion ration (r_e), the correction factor for the critical compression ratio was found and applied.

Figs. 22–25 show the comparison between the simulated results from the GDM and the experimental results. A reference line with a unity gradient is included to illustrate the deviation from the GDM results.

The maximum entrainment ratio (choked secondary flow conditions) obtained from the current experiments and the GDM are compared in Fig. 22. The results for the improved VGRE with an area ratio of 87 were obtained for an expansion ratio ranging from 89 to 167. It was found that the GDM underestimates the entrainment ratio, with a slope of 0.87 giving an average discrepancy of 13 % between the experiments and the simulated entrainment ratio from the GDM.

The results of the critical compression ratio obtained from the experimental data and the GDM are presented in Fig. 23. It was found that the GDM overestimates the critical compression ratio for different expansion ratios, with a slope of 1.34 giving an average discrepancy of 34 % between the experiments and the simulated critical compression ratio from the GDM.

A comparison of the maximum entrainment ratio obtained from the current experiments and the GDM for different ejector area ratios is presented in Fig. 24. The results were obtained for ejector area ratios ranging from 56 to 109 with a primary pressure of 250 kPa and secondary pressure of 1.8 kPa. The GDM was found to underestimate the entrainment ratio for all tested ejector area ratios, with a slope of 0.83 giving an average discrepancy of 17 % between the experiments and the simulated entrainment ratio from the GDM.

The results of the critical compression ratio obtained from the experimental data and the GDM for different ejector area ratios are presented in Fig. 25. It was found that the GDM overestimates the critical compression ratio for all tested ejector area ratios, with a slope of 1.39 giving an average discrepancy of 39 % between the experiments and the simulated critical compression ratio from the GDM.

In conclusion, the comparison between the simulated results from the GDM and the experimental results in Figs. 22–25 showed systematic departures, leading to the conclusion that the GDM was not entirely satisfactory in predicting the performance of the improved VGRE.

5.2. Comparison with previous studies

Fig. 26 depicts the maximum entrainment ratio of the present work in comparison to previous air ejector studies with scaling factors applied to the results of the present GDM in order to achieve an approximate match to the experiments. Based on the scaling factors noted in the legend it is observed that the experimental data falls below the simulated results from GDMs in the work of Hemidi et al. [61], Mazzelli et al. [62], and Rahimi [28] the scaling factors are all less than unity. However, the experimental data of the present work and the work of Alsafi [54] were underestimated by the simulated results obtained from GDM the scaling factors are greater than unity. The difference in entrainment ratio may be due to differences in operating conditions, working fluid properties, and ejector geometry parameters that significantly impact ejector performance.

Fig. 27 illustrates the comparison of critical compression ratio data of the present work with previous air ejector studies with scaled GDM results also included. Based on the scaling factors shown in the legend, which are all less than unity, it is noted that the GDM overestimated the critical compression ratio performance, with the data from the present work and other studies falling below the simulated results in all cases.

Fig. 28 presents the comparison of isentropic efficiency of the improved VGRE with previous air ejector studies for different expansion ratios. The improved VGRE showed significantly better isentropic efficiency than the fixed geometry ejectors, with an average isentropic efficiency of 31.3 %. This demonstrates that the improved VGRE exhibits

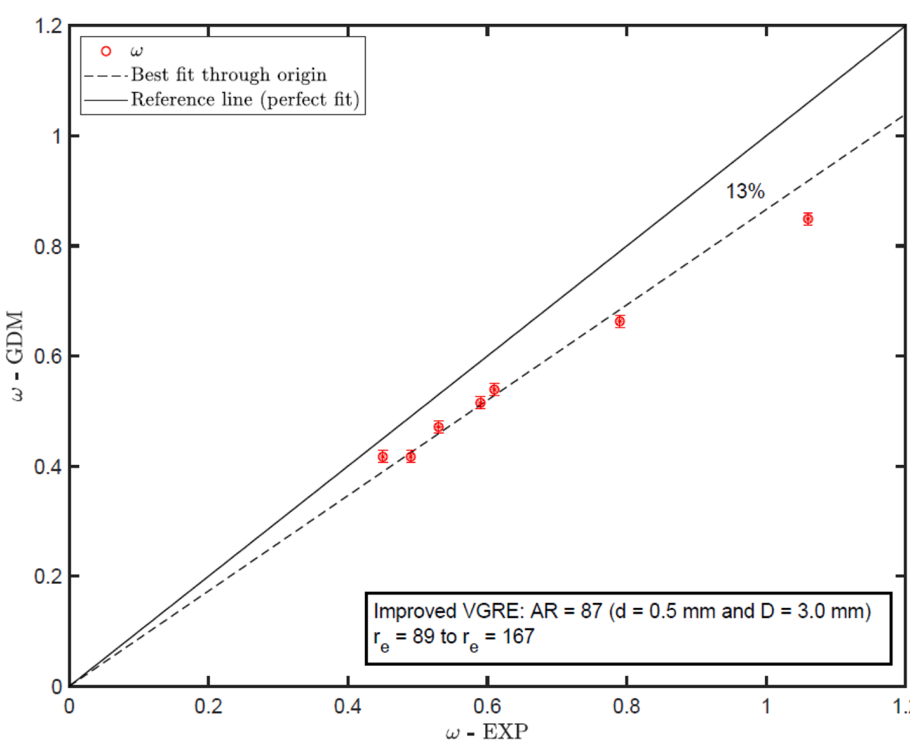

Fig. 22. Experimental and gas dynamic model data comparison for maximum entrainment ratio at various expansion ratios ranging from 89 to 167.

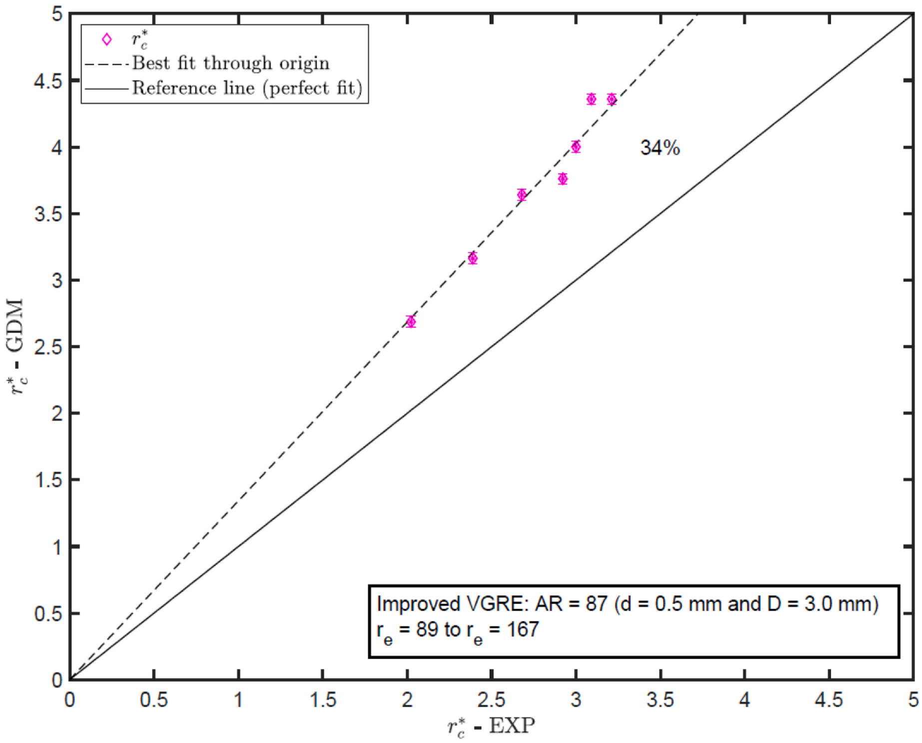

Fig. 23. Comparison of experimental data with a gas dynamic model for critical compression ratio under different expansion ratios ranging from 89 to 167.

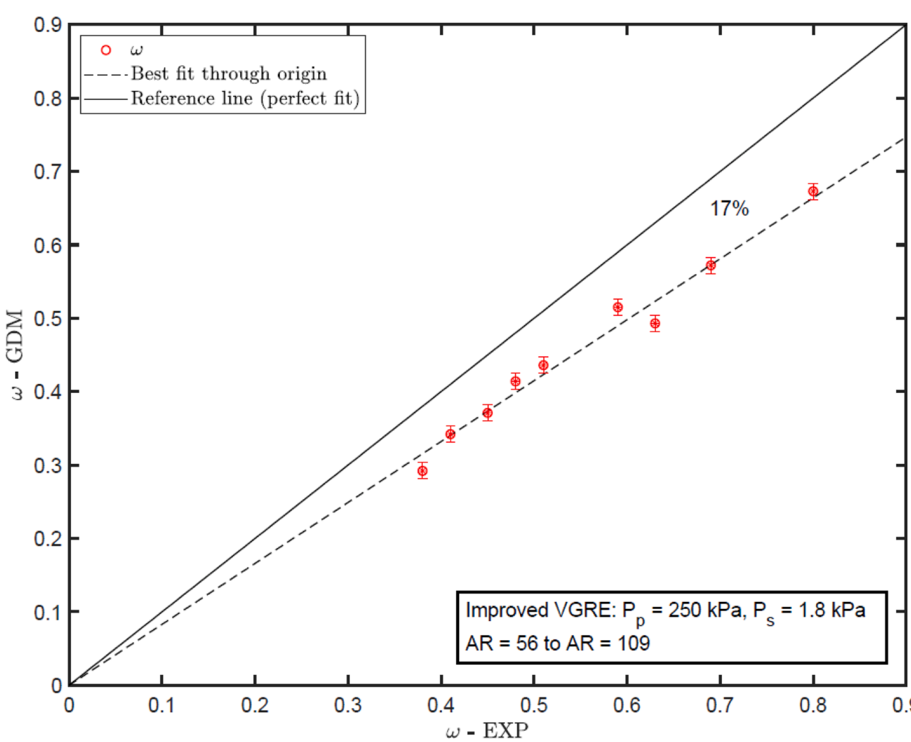

Fig. 24. Comparison of experimental data and gas dynamic model for maximum entrainment ratio for various ejector area ratios in the improved VGRE.

better performance in terms of isentropic efficiency compared to the other fixed geometry ejectors, with Alsafi [54] having an average isentropic efficiency of 26.5 % and Rahimi [28] having an average isentropic efficiency of 5.7 %.

6. Conclusion

The current study focuses on improving the performance of ejectors under varying conditions by developing a radial flow variable geometry ejector (VGRE). The objective of this research is to demonstrate the performance of the improved VGRE. The study investigated the impact of nozzle and duct throat separations on ejector performance, measured

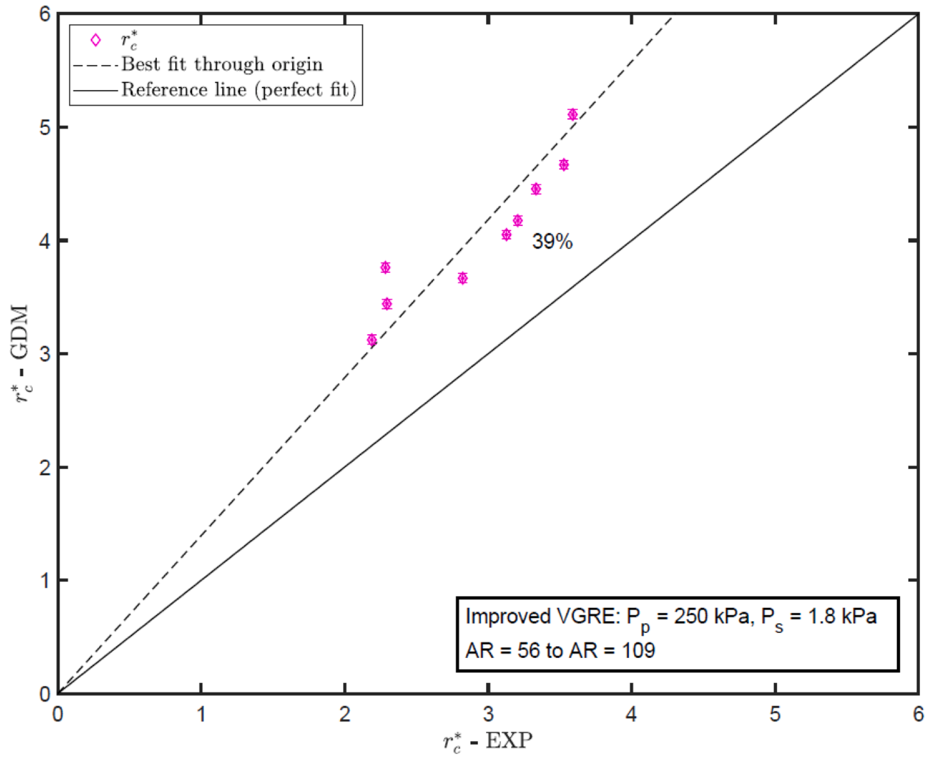

Fig. 25. Comparison of experimental and gas dynamic model data for the critical compression ratio of the improved VGRE at various ejector area ratios.

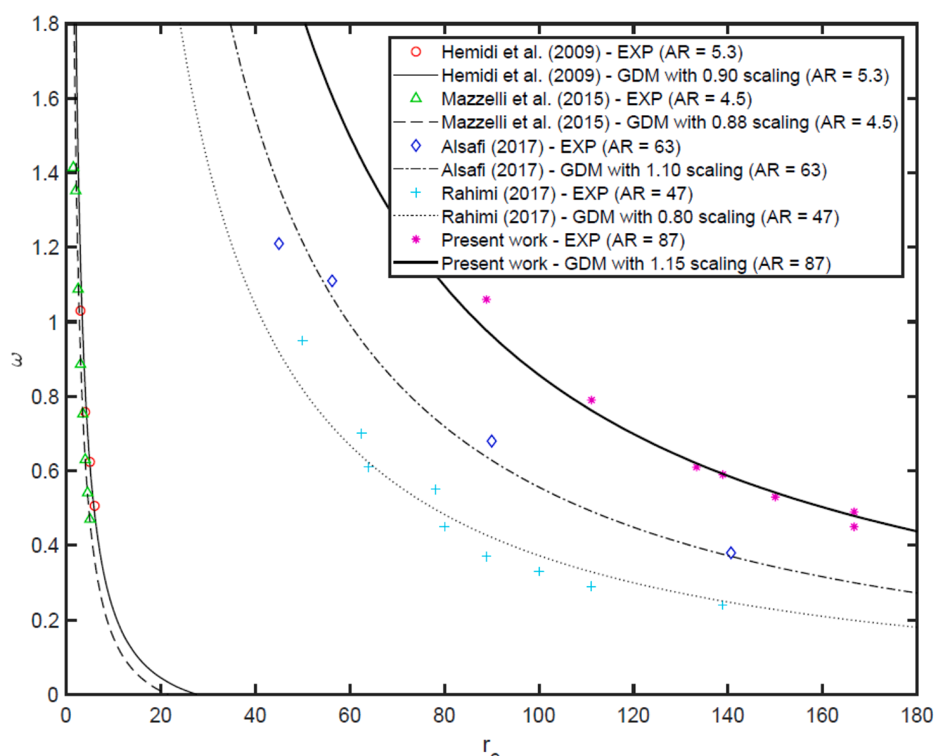

Fig. 26. Comparison between experimental data and gas dynamic modeling: Maximum entrainment ratio variation with expansion ratio in air ejector.

in terms of entrainment ratio and critical compression ratio, under different operating conditions. The results showed that the improved VGRE outperforms a fixed geometry design, offering high performance by selecting the appropriate nozzle and/or duct throat separations. The experiments were conducted using air as the fluid in the ejector and reflect pressure ratios typically encountered in solar cooling applications.

The key findings of the study are:

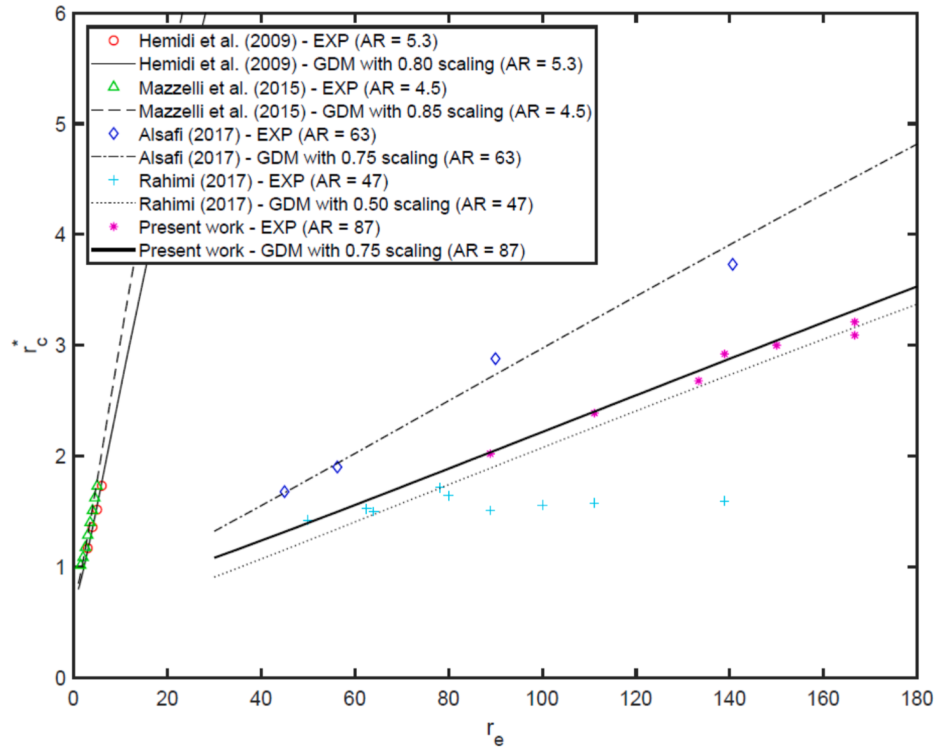

Fig. 27. Comparison of critical compression ratio variation with expansion ratio between air ejector performance data and gas dynamic modelling.

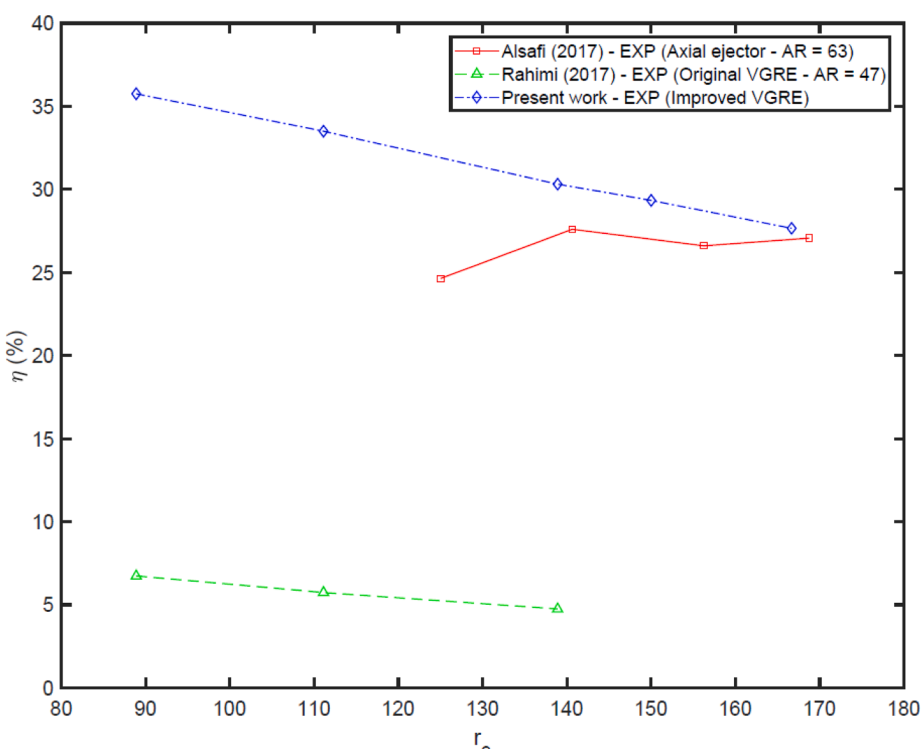

Fig. 28. Isentropic efficiency for various air ejectors at different expansion ratios - comparison of current and previous experimental data.

(1) The optimal performance of the improved VGRE was achieved with nozzle and duct throat separations of 0.5 mm and 3.0 mm, respectively, resulting in an area ratio of 87 and a maximum isentropic ejector efficiency of 36 %. It is expected that optimal performance would occur at different dimensional settings if the range of dimensional change were increased.

(2) The improved VGRE showed an average improvement in entrainment ratio of 146 % and in critical compression ratio of 100 % compared to a single ejector area ratio under different operating conditions. The improved VGRE did not improve performance at the design operating conditions compared to a fixed geometry design.

(3) The wall static pressure in the throat region of the improved VGRE was similar to conventional axial ejectors.
(4) The study found an average discrepancy of 26 % between the experimental results and a theoretical gas dynamic model, and an average increment of 107 % in the entrainment ratio, 76 % in the critical compression ratio, and 18 % in the isentropic efficiency compared to previous studies of air ejectors for the same conditions and axial ejector configurations.

Declaration of Competing Interest

The authors declare that they have no known competing financial interests or personal relationships that could have appeared to influence the work reported in this paper.

Data availability

Data will be made available on request.

References

[1] S. Varga, et al., Preliminary experimental results with a solar driven ejector air conditioner in Portugal, Renew. Energy 109 (2017) 83–92.
[2] M. Hamzaoui, et al., Experimental study of a low grade heat driven ejector cooling system using the working fluid R245fa, Int. J. Refrig. 86 (2018) 388–400.
[3] J. Chen, J. Yu, S. Qian, Subcooling control method for the adjustable ejector in the direct expansion solar assisted ejector-compression heat pump water heater, Appl. Therm. Eng. 148 (2019) 662–673.
[4] H.J. Mosleh, A. Hakkaki-Fard, M. DaqiqShirazi, A year-round dynamic simulation of a solar combined, ejector cooling, heating and power generation system, Appl. Therm. Eng. 153 (2019) 1–14.
[5] B. Tashtoush, Y. Nayfeh, Energy and economic analysis of a variable-geometry ejector in solar cooling systems for residential buildings, J. Storage Mater. 27 (2020), 101061.
[6] E. Gençer, R. Agrawal, Synthesis of efficient solar thermal power cycles for baseload power supply, Energ. Conver. Manage. 133 (2017) 486–497.
[7] A.B. Little, S. Garimella, A critical review linking ejector flow phenomena with component- and system-level performance, Int. J. Refrig. 70 (2016) 243–268.
[8] A. Ramesh, S.J. Sekhar, Experimental and numerical investigations on the effect of suction chamber angle and nozzle exit position of a steam-jet ejector, Energy 164 (2018) 1097–1113.
[9] G. Chen, et al., An improved cascade mechanical compression–ejector cooling cycle, Energy 170 (2019) 459–470.
[10] V.V. Nguyen, et al., Applying a variable geometry ejector in a solar ejector refrigeration system, Int. J. Refrig. (2020).
[11] H. Kim, et al., Computational analysis of a variable ejector flow, J. Therm. Sci. 15 (2) (2006) 140–144.
[12] S. Varga, A.C. Oliveira, B. Diaconu, Influence of geometrical factors on steam ejector performance – A numerical assessment, Int. J. Refrig. 32 (7) (2009) 1694–1701.
[13] X. Ma, et al., Experimental investigation of a novel steam ejector refrigerator suitable for solar energy applications, Appl. Therm. Eng. 30 (11–12) (2010) 1320–1325.
[14] R. Yen, et al., Performance optimization for a variable throat ejector in a solar refrigeration system, Int. J. Refrig. 36 (5) (2013) 1512–1520.
[15] K. Zhang, S. Shen, Y. Yang, Numerical investigation on performance of the adjustable ejector, Int. J. Low-Carbon Technol. 5 (2) (2010) 51–56.
[16] C. Lin, et al., The characteristics of pressure recovery in an adjustable ejector multi-evaporator refrigeration system, Energy 46 (1) (2012) 148–155.
[17] C. Lin, et al., Numerical investigation of geometry parameters for pressure recovery of an adjustable ejector in multi-evaporator refrigeration system, Appl. Therm. Eng. 61 (2) (2013) 649–656.
[18] Y. Jeon, et al., Effects of ejector geometries on performance of ejector-expansion R410A air conditioner considering cooling seasonal performance factor, Appl. Energy 205 (2017) 761–768.
[19] N. Ruangtrakoon, S. Aphornratana, T. Sriveerakul, Experimental studies of a steam jet refrigeration cycle: effect of the primary nozzle geometries to system performance, Exp. Therm. Fluid Sci. 35 (4) (2011) 676–683.
[20] P.R. Pereira, et al., Experimental results with a variable geometry ejector using R600a as working fluid, Int. J. Refrig. 46 (2014) 77–85.
[21] R. Yapıcı, H. Ersoy, Performance characteristics of the ejector refrigeration system based on the constant area ejector flow model, Energ. Conver. Manage. 46 (18–19) (2005) 3117–3135.
[22] M.A. Al-Nimr, B. Tashtoush, A. Hasan, A novel hybrid solar ejector cooling system with thermoelectric generators, Energy 198 (2020), 117318.
[23] K. Cizungu, M. Groll, Z. Ling, Modelling and optimization of two-phase ejectors for cooling systems, Appl. Therm. Eng. 25 (13) (2005) 1979–1994.
[24] Y. Zhu, et al., Numerical investigation of geometry parameters for design of high performance ejectors, Appl. Therm. Eng. 29 (5–6) (2009) 898–905.
[25] C. Li, Y. Li, L. Wang, Configuration dependence and optimization of the entrainment performance for gas–gas and gas–liquid ejectors, Appl. Therm. Eng. 48 (2012) 237–248.
[26] M. Palacz, et al., Shape optimisation of a two-phase ejector for CO_2 refrigeration systems, Int. J. Refrig. 74 (2017) 212–223.
[27] T. Ng, D. Otis, Experimental investigation of a variable geometry, radial ejector, J. Fluids Eng. 101 (4) (1979) 491–494.
[28] H. Rahimi, Investigation of Radial Flow Ejector Performance through Experiments and Computational Simulations, University of Southern Queensland, 2017.
[29] G. Besagni, N. Cristiani, Multi-scale evaluation of an R290 variable geometry ejector, Appl. Therm. Eng. 188 (2021), 116612.
[30] E.O. Sampedro, A new variable mixing chamber ejector: CFD assessment, Appl. Therm. Eng. 208 (2022), 118242.
[31] J. Chen, et al., A novel control strategy with an anode variable geometry ejector for a SOFC-GT hybrid system, Energy 261 (2022), 125281.
[32] Z. Chen, et al., Synergistic effect of adjustable ejector structure and operating parameters in solar-driven ejector refrigeration system, Sol. Energy 250 (2023) 295–311.
[33] C.A. Garris Jr. et al., A New Thermally Driven Refrigeration System with Environmental Benefits, George Washington University, Washington, DC (US), 1998.
[34] K.M. Tacina, R. Fernandez, S.M. Moody, Thrust augmentation in an unsteady supersonic ejector, in: 42nd AIAA Aerospace Sci. Meeting and Exhibit., Reno, NV, 2004.
[35] A. Ababaneh, et al., Investigation of the Mach number effects on fluid-to-fluid interaction in an unsteady ejector with a radial-flow diffuser, JJMIE 3 (2) (2009) 131–140.
[36] R.H. Al-Rbaihat, Design of Variable Geometry Radial Ejector for HVAC Purposes through Experiments and Simulation, University of Southern Queensland, 2020.
[37] J.A. Kentfield, The Performance of Pressure-Exchanger Dividers and Equalizers, 1969.
[38] R. Al-Rbaihat et al., Detached eddy simulation of an adjustable radial ejector, in: Proceedings of the 21st Australasian Fluid Mechanics Conference, Australasian Fluid Mechanics Society, 2018.
[39] N. Johannesen, Ejector Theory and Experiments, ATS No. 1. Trans., Danish Acad. Tech. Copenhagen, Denmark, 1951.
[40] E. ESDU86030, J. Pumps, Design for Steam Driven Flow, Engineering Sciences Data Unit, London, 1986.
[41] E. Rusly, et al., CFD analysis of ejector in a combined ejector cooling system, Int. J. Refrig. 28 (7) (2005) 1092–1101.
[42] G.F.L. Al-Doori, Investigation of Refrigeration System Steam Ejector Performance through Experiments and Computational Simulations, University of Southern Queensland, 2013.
[43] H. Wu, et al., Numerical investigation of the influences of mixing chamber geometries on steam ejector performance, Desalination 353 (2014) 15–20.
[44] Y. Wu, et al., Optimization analysis of structure parameters of steam ejector based on CFD and orthogonal test, Energy 151 (2018) 79–93.
[45] G.-M. Chen, et al., Experimental investigation of an adjustable ejector for CO_2 heat pump water heaters, J. Zhejiang Univ.-Sci. A 10 (11) (2009) 1678–1682.
[46] T. Thongtip, S. Aphornratana, An experimental analysis of the impact of primary nozzle geometries on the ejector performance used in R141b ejector refrigerator, Appl. Therm. Eng. 110 (2017) 89–101.
[47] M. Poirier, D. Giguère, H. Sapoundjiev, Experimental parametric investigation of vapor ejector for refrigeration applications, Energy 162 (2018) 1287–1300.
[48] B. Tashtoush, M.B. Younes, Comparative thermodynamic study of refrigerants to select the best environment-friendly refrigerant for use in a solar ejector cooling system, Arab. J. Sci. Eng. 44 (2) (2019) 1165–1184.
[49] Y. Han, et al., Characterization of choking flow behaviors inside steam ejectors based on the ejector refrigeration system, Int. J. Refrig. 113 (2020) 296–307.
[50] C. Li, et al., Analysis on performance characteristics of ejector with variable area-ratio for multi-evaporator refrigeration system based on experimental data, Appl. Therm. Eng. 68 (1–2) (2014) 125–132.
[51] Y. Zhu, P. Jiang, Experimental and numerical investigation of the effect of shock wave characteristics on the ejector performance, Int. J. Refrig. 40 (2014) 31–42.
[52] K. Chunnanond, S. Aphornratana, An experimental investigation of a steam ejector refrigerator: the analysis of the pressure profile along the ejector, Appl. Therm. Eng. 24 (2) (2004) 311–322.
[53] K. Pianthong, et al., Investigation and improvement of ejector refrigeration system using computational fluid dynamics technique, Energ. Conver. Manage. 48 (9) (2007) 2556–2564.
[54] M. Alsafi, Constant Rate of Momentum Change Ejector: Simulation, Experiments and Flow Visualisation, University of Southern Queensland, 2017.
[55] H. Xue, et al., Design and investigation of a two-stage vacuum ejector for MED-TVC system, Appl. Therm. Eng. 167 (2020), 114713.
[56] B. Tashtoush, A.B.R. Algharbawi, Parametric study of a novel hybrid solar variable geometry ejector cooling with organic Rankine cycles, Energ. Conver. Manage. 198 (2019), 111910.
[57] S. Mohamed, Y. Shatilla, T. Zhang, CFD-based design and simulation of hydrocarbon ejector for cooling, Energy 167 (2019) 346–358.
[58] W. Gu, et al., Performance investigation of an auto-tuning area ratio ejector for MED-TVC desalination system, Appl. Therm. Eng. (2019).
[59] B. Elhub, et al., Performance evaluation and parametric studies on variable nozzle ejector using R134A, Case Stud. Therm. Eng. 12 (2018) 258–270.

[60] D. Buttsworth, Calibration of a gas dynamic model for ejector performance, in: ASTFE Digital Library, Begel House Inc., 2017.
[61] A. Hemidi, et al., CFD analysis of a supersonic air ejector. Part II: relation between global operation and local flow features, Appl. Therm. Eng. 29 (14–15) (2009) 2990–2998.
[62] F. Mazzelli, et al., Computational and experimental analysis of supersonic air ejector: turbulence modeling and assessment of 3D effects, Int. J. Heat Fluid Flow 56 (2015) 305–316.